Progress In Electromagnetics Research B, Vol. 78, 91–124, 2017

Modelling and Validation of Combined Active and Passive Microwave Remote Sensing of Agricultural Vegetation at L-Band

Huanting Huang[1, *], Tien-Hao Liao[2], Leung Tsang[1], Eni G. Njoku[2], Andreas Colliander[2], Thomas J. Jackson[3], Mariko S. Burgin[2], and Simon Yueh[2]

Abstract—The distorted Born approximation (DBA) of volume scattering was previously combined with the numerical solution of Maxwell equations (NMM3D) for rough surfaces to calculate radar backscattering coefficients for the Soil Moisture Active Passive (SMAP) mission. The model results were validated with the Soil Moisture Active Passive Validation Experiment 2012 (SMAPVEX12) data. In this paper we extend the existing model to calculate the bistatic scattering coefficients for each of the three scattering mechanisms: volume, double bounce and surface scattering. Emissivities are calculated by integrating the bistatic scattering coefficients over the hemispherical solid angle. The backscattering coefficients and emissivities calculated using this approach form a consistent model for combined active and passive microwave remote sensing. This has the advantage that the active and passive microwave remote sensing models are founded on the same theoretical basis and hence allow the use of the same physical parameters such as crop density, plant height, stalk orientation, leaf radius, and surface roughness, amongst others. In this paper, this combined active and passive model, DBA/NMM3D, is applied to four vegetation types to calculate both backscattering coefficients and brightness temperature: wheat, winter wheat pasture and canola. This model uses a single-scattering and incoherent vegetation model which is applicable for the vegetation fields studied in this paper but not suitable for vegetation types where collective scattering or multiple scattering effects are important. We demonstrate the use of the DBA/NMM3D for both active and passive using the same input parameters for matching active and passive coincident data. The model results are validated using coincident airborne Passive Active L-band System (PALS) low-altitude radiometer data and Uninhabited Aerial Vehicle Synthetic Aperture Radar (UAVSAR) data taken during the SMAPVEX12 field campaign. Results show an average root mean squared error (RMSE) of 1.04 dB and 1.21 dB for backscatter at VV and HH, respectively, and 4.65 K and 6.44 K for brightness temperature at V-pol and H-pol, respectively. The results are comparable to those from the tau-omega model which is commonly used to compute the brightness temperature, though the physical parameters used in this model are different from the empirically adjusted parameters used in the tau-omega model.

1. INTRODUCTION

Combined active and passive microwave remote sensing of vegetated surfaces is of great interest and importance given the increasing number of active and passive satellite microwave missions and datasets available for studies of land surfaces for application in hydrology and terrestrial ecology [1]. For example, L-band radar and radiometer data can be used to retrieve soil moisture over crop fields. According to the previous research, L-band is the optimal choice for remote sensing of near surface soil moisture of

Received 3 June 2017, Accepted 9 August 2017, Scheduled 25 August 2017

* Corresponding author: Huanting Huang (huanght@umich.edu).

[1] Radiation Laboratory, Department of Electrical Engineering and Computer Science, University of Michigan, Ann Arbor, MI 48109, USA. [2] Jet Propulsion Laboratory, California Institute of Technology, Pasadena, CA 91109, USA. [3] USDA, Agricultural Research Service, Hydrology and Remote Sensing Laboratory, Beltsville, MD 20705, USA.

vegetated surfaces with moderate vegetation water content (VWC) [2, 3]. At L-band, the atmosphere can be near transparent even under cloudy and rain conditions and the transmissivity through the vegetation canopy with moderate VWC is relatively high; so that the L-band radar or radiometer data has considerable sensitivity to the near surface soil moisture of the agricultural fields [2–5]. Soil moisture is closely linked to crop water stress and its availability hence provides better crop supply and demand information. This in turn enables improvements in crop productivity [5]. The VWC is closely related to the crop development and can also be estimated from the radar and radiometer data. This further enables crop assessment and monitoring [5]. For many years, passive microwave retrieval algorithms for satellite missions such as Advanced Microwave Scanning Radiometer-E (AMSR-E), Soil Moisture Ocean Salinity (SMOS), and SMAP have been based on the tau-omega model [6, 7], which is derived from a zeroth order solution of the radiative transfer equation. Since the zeroth order solution ignores the phase matrix term [8], an empirically adjusted scattering albedo ω, which is usually smaller than the physical parameter, must be used to fit this model to observations. The vegetation parameter b used in the tau-omega model to relate VWC to the optical thickness τ is also empirical. In modelling the rough surface effects in the tau-omega model, the h-Q formulation [9] is used; it includes only the coherent wave specular reflection while ignoring the bistatic scattering. Thus, empirical "best-fit" parameters rather than physical parameters are used in the tau-omega model. For active remote sensing modelling, we previously used the distorted Born approximation (DBA) [10] and the numerical solutions of the Maxwell equations (NMM3D) [11] (this method is called NMM3D-DBA for short), where the coherent reflectivity and rough surface scattering are calculated by NMM3D [12]. This model was used to calculate the VV and HH backscatter at L-band for pasture [13], wheat, winter wheat and canola fields. The active model has been validated using data from the Soil Moisture Active Passive Validation Experiment 2012 (SMAPVEX12) [13, 14]. The distorted Born approximation is valid for these vegetation types because the optical thickness at L-band is small.

Combined active and passive approaches for remote sensing of vegetated surfaces have been studied extensively. In many studies, the analyses for radiometer and radar data were based on different models: the tau-omega model was used as a passive model [15, 16], while an empirical model [15] or the water-cloud model [16] was used as an active model. Ferrazzoli et al. [17] and Guerriero et al. [18] discussed the interrelations between emission and scattering for vegetated surfaces. In [17, 18], the emissivity and backscattering coefficient were computed in a unified approach using the radiative transfer theory and the "matrix doubling" algorithm. Chauhan et al. [19] used DBA to compute both the backscattering coefficient and brightness temperature for corn. But the direct scattering from the soil surface was not taken into account, which can be important for rough soil surface [20]. Furthermore, only brightness temperature data at H-polarization over a one-week period were used for comparison. In this paper, we study active and passive microwave remote sensing in a consistent manner using NMM3D-DBA for both active and passive. The active model NMM3D-DBA is extended to calculate bistatic scattering, and integration of the bistatic scattering over the hemispherical solid angle is used to calculate emissivity. Thus, the active and passive microwave remote sensing models are founded on the same theoretical basis and allow the use of the same physical parameters such as crop density, plant height, stalk orientation, leaf radius, surface roughness, amongst others. The vegetation canopy is modeled as a layer of uniformly distributed dielectric cylinders and disks representing stalks and leaves, respectively [10]. The distorted Born approximation is derived from the Foldy-Lax equation with first-order iteration using the half-space Green's function and T-matrix [8]. The attenuation through the vegetation layer is accounted for by the imaginary part of the effective propagation constant calculated by Foldy's approximation [8]. NMM3D results are based on the Method of Moments (MoM) with the Rao-Wilton-Glisson (RWG) basis function using Gaussian random rough surfaces with exponential correlation functions, which have been shown to agree well with experimental data for various root mean square (RMS) height values and soil moisture conditions [11]. The total bistatic scattering is expressed as the incoherent sum of three scattering mechanisms: volume scattering, double bounce scattering and surface scattering. In the coherent model [21–23], the collective scattering between the vegetation scatterers is taken into account, and then the scattering from the vegetation and the scattering from the rough surface are added incoherently. The coherent model is more difficult to implement than the incoherent model, especially for calculating emissivity which includes integration over the upper hemispherical solid angle. The coherent model also requires more input parameters such as the relative positions of the scatterers.

In this paper, it is the first time that the incoherent model is combined with NMM3D for emissivity calculations. The MIMICS model [24] uses first order radiative transfer (RT) and the rough surface scattering is calculated by one of the three methods: Geometrical Optical Model (GO), Physical Optics Model (PO) and Small Perturbation Method (SPM). In this paper, we use NMM3D-DBA. The DBA is the same as the first order RT theory except that it includes backscattering enhancement [25] in the double-bounce term. In the backscattering direction, the double-bounce term from DBA is twice (3 dB) larger than that from the first order RT for co-pol. The rough surface scattering is calculated by the numerical solution of Maxwell equations (NMM3D).

Here, the NMM3D-DBA model is applied to the analysis of SMAPVEX12 data for wheat, winter wheat, pasture and canola fields to calculate both brightness temperatures and radar backscatter coefficients. The collective and multiple scattering effects do not contribute significantly for the fields studied in the paper since bistatic surface scattering mostly dominates among the three scattering mechanisms and the scattering parameter ω as well as the optical thickness τ is not large for these fields. Thus the distorted Born approximation which is easier to implement and requires less input parameters than the coherent model [21] and the multiple scattering model [26] is applied to these fields. The model results are compared with the brightness temperature and backscatter observations from SMAPVEX12 [14]. SMAPVEX12 was a pre-launch Soil Moisture Active Passive (SMAP) field experiment. Observations began during the period of early crop development and finished at the point where crops had reached maximum biomass. Soil moisture also varied significantly [14]. These long-duration measurements, over a wide range of soil moisture and vegetation conditions, are a unique and valuable attribute of this field campaign when compared with previous airborne experiments, and provide an extensive data set critical to test the vegetation scattering models and radar-based soil moisture retrieval algorithm for SMAP [14].

The outline of the paper is as follows: In Section 2, we derive the bistatic scattering coefficients using NMM3D-DBA that are used to calculate the emissivity. Section 3 describes the SMAPVEX12 campaign data that provide the input parameters and comparisons for the model. Next, the NMM3D-DBA model uses the same physical parameters to compute both brightness temperature and backscatter, which are evaluated by the SMAPVEX12 Passive Active L-band System (PALS) low-altitude radiometer data and Uninhabited Aerial Vehicle Synthetic Aperture Radar (UAVSAR) data, respectively in Section 4. Section 5 presents the comparison of the NMM3D-DBA and the tau-omega model.

2. COMBINED ACTIVE AND PASSIVE MODEL (NMM3D-DBA)

Emissivity (e_q) related to brightness temperature through the physical temperature of the object, is calculated by integrating the bistatic scattering coefficients over the hemispherical solid angle as given in Equation (1) [17, 18]

$$e_q = 1 - \frac{1}{4\pi} \int_0^{\pi/2} d\theta_s \sin\theta_s \int_0^{2\pi} d\phi_s \sum\nolimits_{p=v \text{ or } h} \gamma_{pq}\left(\theta_s, \phi_s; \theta_i, \phi_i\right) \tag{1}$$

where the subscripts 'p' and 'q' stand for polarization, either 'v' or 'h'. γ_{pq} is the bistatic scattering coefficient with 'q' denoting the polarization of transmitting and 'p' denoting the polarization of receiving. θ_i and ϕ_i as used in a spherical coordinate system define the incident direction, while θ_s and ϕ_s define the scattering direction. The integration is calculated numerically using the Trapezoid rule. The convergence of the integration with regard to the number of points used has been checked. To calculate the bistatic scattering coefficient γ we use the distorted Born approximation for the vegetation volume scattering and NMM3D [11] for coherent reflectivity and bistatic rough surface scattering of the soil surface. In the derivations below, the crucial assumptions are: (1) the vegetation scatterers are uniformly distributed in the vegetation layer; (2) each type of vegetation scatterer, such as stalks or leaves, is statistically identical in terms of the size, shape and permittivity; (3) there is no correlation between the scattered fields of different vegetation scatterers, hence the incoherent model can be used; and (4) the first-order scattering contributions are significantly larger than the high-order scattering contributions in the vegetation, such that a single scattering approximation is applicable.

As shown in Figure 1, let the vegetation layer be region 1 and the air above the vegetation layer be region 0. Then, the total field in region 0 is according to the Foldy-Lax equation [8] with first-order

iteration:

$$\overline{E} = \overline{E}_{inc} + \overline{E}_{ref} + \sum_{j=1}^{N} \overline{\overline{G}}_{01} \overline{\overline{T}}_j \left(\overline{E}_{inc} + \overline{E}_{ref} \right) \tag{2}$$

where N is the total number of scatterers, and $\overline{\overline{T}}_j$ is the transfer operator for scatterer j [8]. The subscript '01' of the Green's function ($\overline{\overline{G}}_{01}$) indicates that the scatterers are in region 1 while the observation is in region 0. $\overline{E}_{inc}$ and $\overline{E}_{ref}$ are the incident field and reflected field by the rough surface under the vegetation, respectively.

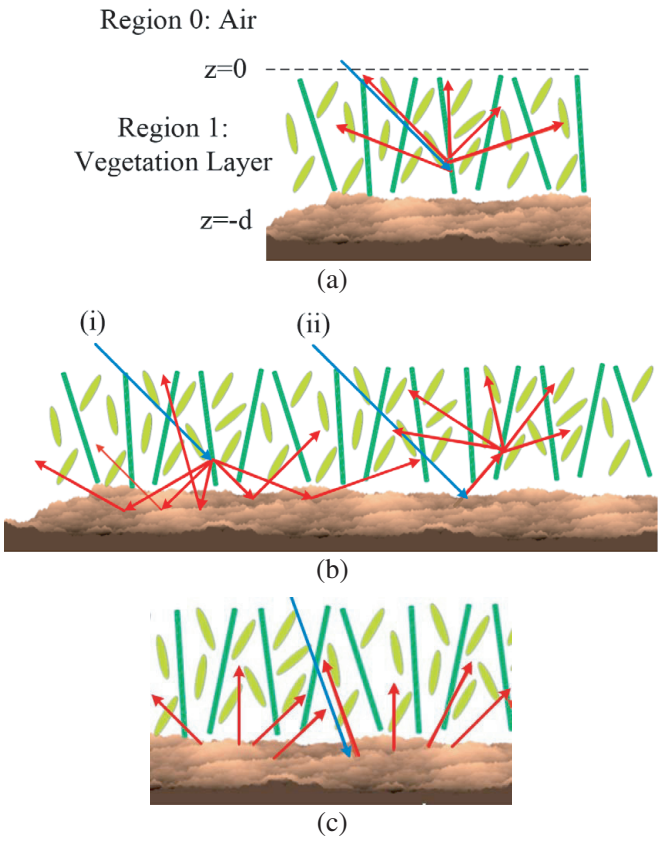

Figure 1. Scattering from a vegetated surface. The three scattering mechanisms are: (a) volume scattering; (b) double-bounce scattering (i) scattering from the scatterer and then reflected by the surface, (ii) scattering of the reflected wave by a scatterer; (c) surface scattering.

The vegetation scatterers are in the upper space over a lower space of soil, as shown in Figure 1. There is reflection at the boundary between the vegetation layer and the soil while there is no physical reflection at $z = 0$ (between the vegetation layer and air). Thus, the half space Green's function [8] is used and can be separated into two terms ($\overline{\overline{G}}_{01}^{(0)}$ and $\overline{\overline{G}}_{01}^{(R)}$ as below). The total scattered field from the N vegetation particles can be written as [8]:

$$\overline{E}_s = \sum_{j=1}^{N} \overline{\overline{G}}_{01} \overline{\overline{T}}_j \left(\overline{E}_{inc} + \overline{E}_{ref} \right) = \sum_{j=1}^{N} \left(\overline{\overline{G}}_{01}^{(0)} + \overline{\overline{G}}_{01}^{(R)} \right) \overline{\overline{T}}_j \left(\overline{E}_{inc} + \overline{E}_{ref} \right) \tag{3a}$$

where $\overline{\overline{G}}_{01}^{(R)}$ with the superscript '(R)' represents the part of Green's function with reflection by the soil below while $\overline{\overline{G}}_{01}^{(0)}$ with the superscript '(0)' represents the remainder of the Green's function.

Multiplying out the two brackets yields

$$\overline{E}_s = \sum_{j=1}^{N} \left(\overline{\overline{G}}_{01}^{(0)} \overline{\overline{T}}_j \overline{E}_{inc} + \overline{\overline{G}}_{01}^{(R)} \overline{\overline{T}}_j \overline{E}_{inc} + \overline{\overline{G}}_{01}^{(0)} \overline{\overline{T}}_j \overline{E}_{ref} + \overline{\overline{G}}_{01}^{(R)} \overline{\overline{T}}_j \overline{E}_{ref} \right) \tag{3b}$$

$$\overline{E}_s \approx \sum_{j=1}^{N} \left(\overline{\overline{G}}_{01}^{(0)} \overline{\overline{T}}_j \overline{E}_{inc} + \overline{\overline{G}}_{01}^{(R)} \overline{\overline{T}}_j \overline{E}_{inc} + \overline{\overline{G}}_{01}^{(0)} \overline{\overline{T}}_j \overline{E}_{ref} \right) \tag{3c}$$

The first term ($\sum_{j=1}^{N} \overline{\overline{G}}_{01}^{(0)} \overline{\overline{T}}_j \overline{E}_{inc}$) in Equation (3b) is the volume scattering while the second and third terms ($\sum_{j=1}^{N} \overline{\overline{G}}_{01}^{(R)} \overline{\overline{T}}_j \overline{E}_{inc}$ and $\sum_{j=1}^{N} \overline{\overline{G}}_{01}^{(0)} \overline{\overline{T}}_j \overline{E}_{ref}$) are the double-bounce scattering, as illustrated in Figures 1(a) and (b). The last term ($\sum_{j=1}^{N} \overline{\overline{G}}_{01}^{(R)} \overline{\overline{T}}_j \overline{E}_{ref}$) in Equation (3b) is the triple bounce scattering, which is likely to be weak in the case of grass, wheat, canola and soybean fields at L-band [27]; it is ignored here as shown in Equation (3c).

According to the analysis above, the total bistatic scattering is calculated as the sum of the three scattering mechanisms shown in Figure 1: volume scattering, double bounce scattering and surface scattering.

$$\gamma_{pq} = \gamma_{pq}^{vol} + \gamma_{pq}^{db} + \gamma_{pq}^{surf} \tag{4}$$

where the superscript '*vol*' is short for volume scattering, '*db*' short for double bounce scattering and '*surf*' short for surface scattering.

The bistatic scattering coefficient is calculated as [4]:

$$\gamma_{pq} = \frac{4\pi}{A \cos\theta_i} \left\langle S_{pq} S_{pq}^* \right\rangle \tag{5}$$

where A is the illumination area, and S_{pq} is the element in the scattering matrix. The angle bracket $\langle\rangle$ in the expression indicates the statistical average over the orientations of different scatterers. The calculations of S_{pq} are detailed in the Appendix.

The S_{pq} for volume scattering is

$$S_{pq}^{vol} = \sum_{j=1}^{N} \exp\left(-i\left(\overline{k}_{sp} - \overline{K}_{iq}\right) \cdot \overline{r}_j\right) f_{pq,j}\left(\theta_s, \phi_s; \pi - \theta_i, \phi_i\right) \tag{6}$$

with,

$$\overline{k}_{sp} = k\sin\theta_s\cos\phi_s\hat{x} + k\sin\theta_s\sin\phi_s\hat{y} + k_{spz}\hat{z}, \quad \overline{K}_{iq} = k\sin\theta_i\cos\phi_i\hat{x} + k\sin\theta_i\sin\phi_i\hat{y} - k_{iqz}\hat{z} \tag{7}$$

where the subscript 'i' represents incident and is changed to 's' when representing scattered. $\overline{r}_j = x_j\hat{x} + y_j\hat{y} + z_j\hat{z}$ is the position of the jth scatterer. k is the wavenumber in free space. $f_{pq,j}$ is the scattering amplitude for the jth scatterer. Cylinders and disks are used to model the vegetation scatterers [10]. For example, grass, wheat and the stalks of the canola plants are modeled as cylinders while canola leaves are modeled as disks as shown in Figures 2–4 and Figure 5(a). The scattering amplitudes $f_{pq,j}$ for cylinders and disks are calculated using the Infinite Cylinder Approximation (ICA) and Generalized Rayleigh-Gans Approximation [8], respectively.

The boundary condition, which is also called the phase matching condition, states that the tangential component of the total electric field is continuous across the boundary when there are no sources at the boundary [4]. With the application of the phase matching condition [4] at the boundary between the air and vegetation layer, it is obtained that

$$k_{iqz} = \sqrt{k_q^2 - k^2\sin^2\theta_i} \tag{8}$$

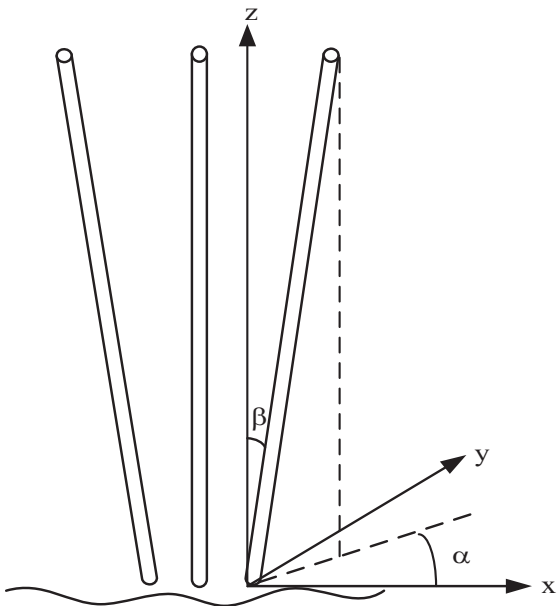

Figure 2. Cylindrical scatterer elevation angle (β) and azimuth angle (α).

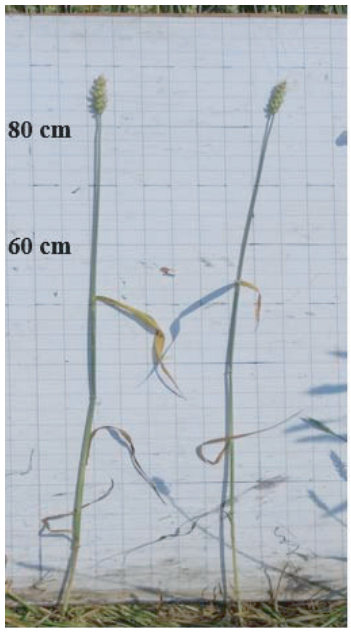

Figure 3. Photos of wheat from SMAPVEX12.

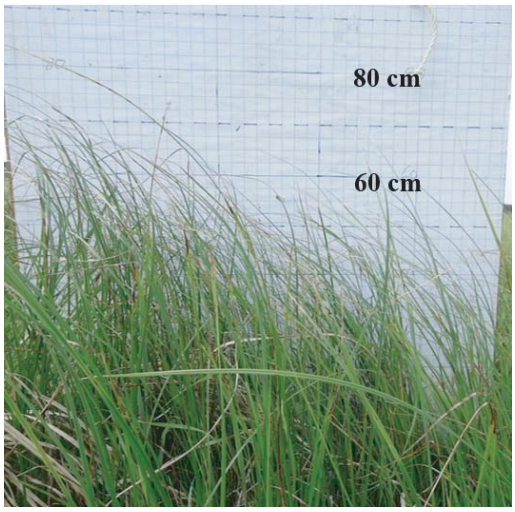

Figure 4. Photos of pasture from SMAPVEX12.

where k_q is the effective propagation constant in the vegetation layer for polarization 'q'. k_q is calculated by Foldy's approximation where the scatterers are treated as embedded in the equivalent homogenous media [8],

$$k_q = k + \frac{2\pi n_0}{k} \langle f_{qq}(\pi - \theta_i, 0; \pi - \theta_i, 0) \rangle \tag{9}$$

where n_0 is the number of scatterers per m^3.

k_{spz} is obtained in the same way. Using Equation (6) and assuming independent scattering,

$$\left\langle S_{pq}^{vol} S_{pq}^{vol*} \right\rangle = \sum_{j=1}^{N} \left\{ \begin{array}{l} \left\langle \exp\left(-i\left(\overline{k}_{sp} - \overline{K}_{iq}\right) \cdot \overline{r}_j\right) \exp\left(i\left(\overline{k}_{sp}^* - \overline{K}_{iq}^*\right) \cdot \overline{r}_j\right) \right\rangle \\ \times \left\langle f_{pq,j}(\theta_s, \phi_s; \pi - \theta_i, \phi_i) f_{pq,j}^*(\theta_s, \phi_s; \pi - \theta_i, \phi_i) \right\rangle \end{array} \right\} \tag{10}$$

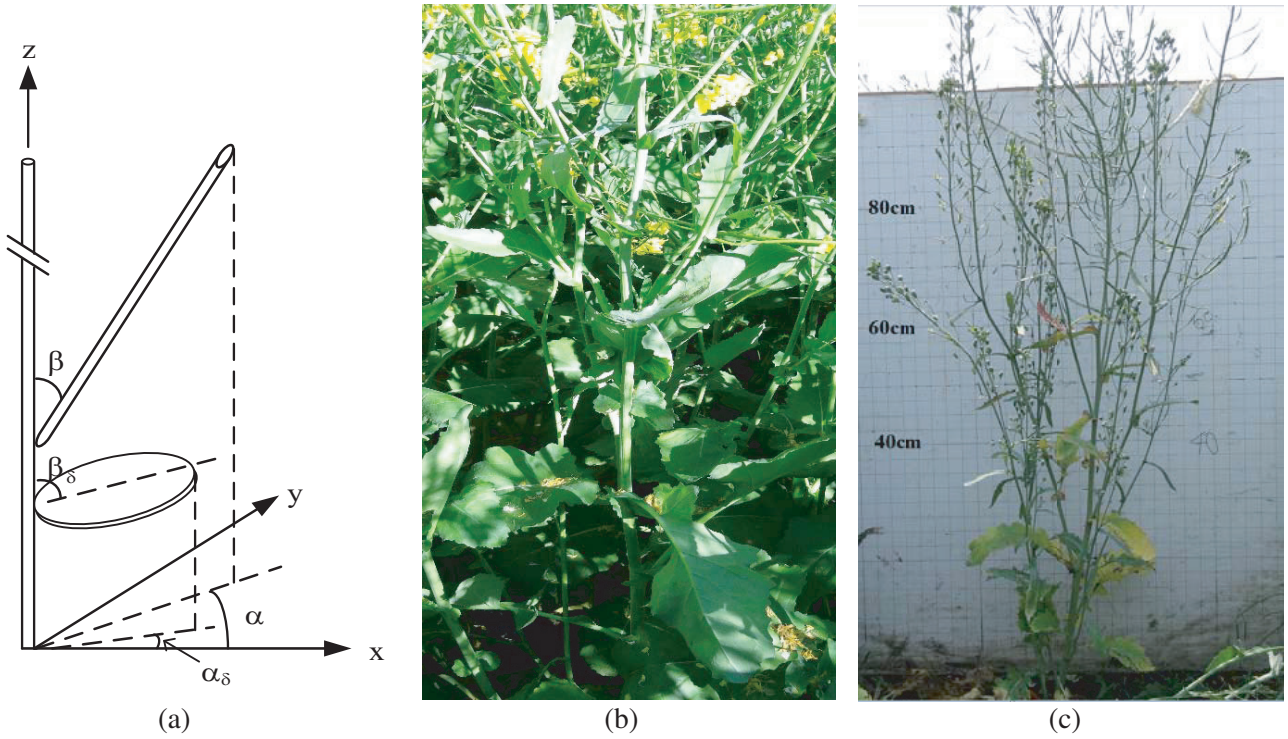

(a) (b) (c)

Figure 5. (a) Canola model. Photos of canola from SMAPVEX12 taken on (b) June 25, (c) July 17.

Assuming that the scatterers are statistically identical and uniformly distributed in the vegetation layer [8], we can rewrite Equation (10) as:

$$\left\langle S_{pq}^{vol} S_{pq}^{vol*} \right\rangle = \frac{N}{V} \int d\overline{r}_j \exp\left(2\mathrm{Im}\left(\overline{k}_{sp} - \overline{K}_{iq}\right) \cdot \overline{r}_j\right) \left\langle \left| f_{pq}\left(\theta_s, \phi_s; \pi - \theta_i, \phi_i\right)\right|^2 \right\rangle \tag{11}$$

where V is the volume of the vegetation layer, and Im() indicates that only the imaginary part is used. According to the phase matching condition [4], the x and y components of $\overline{k}_{sp}$ and $\overline{K}_{iq}$ are real and only the z component has an imaginary part. Use the relationship that $\frac{N}{V} = n_0$. Let the thickness of the vegetation layer be d, and then it follows that:

$$\left\langle S_{pq}^{vol} S_{pq}^{vol*} \right\rangle = n_0 A \int_{-d}^{0} \exp\left(2\mathrm{Im}\left(k_{spz} - K_{iqz}\right) z_j\right) \left\langle \left| f_{pq}\left(\theta_s, \phi_s; \pi - \theta_i, \phi_i\right)\right|^2 \right\rangle dz_j \tag{12}$$

where z_j is the z coordinate of the jth scatterer. The limits of the integration is $-d$ and 0 since the vegetation layer is within the range of $-d$ to 0 as illustrated in Figure 1.

And finally by substituting Equation (12) into (5),

$$\gamma_{pq}^{vol} = \frac{4\pi n_0}{\cos\theta_i} \frac{1 - \exp\left(-2\left(\mathrm{Im}\left(k_{spz}\right) + \mathrm{Im}\left(k_{iqz}\right)\right) d\right)}{2\left(\mathrm{Im}\left(k_{spz}\right) + \mathrm{Im}\left(k_{iqz}\right)\right)} \left\langle \left| f_{pq}\left(\theta_s, \phi_s; \pi - \theta_i, \phi_i\right)\right|^2 \right\rangle \tag{13}$$

Next, for double bounce scattering, there are two terms: (i) scattering from a scatterer that is then reflected by the surface, and (ii) scattering of the reflected wave by a scatterer, as shown in Figure 1(b). The bistatic scattering coefficient for double bounce scattering is thus the sum of the bistatic scattering coefficient of these two scattering terms:

$$\gamma_{qp}^{db} = \gamma_{qp}^{db,sr} + \gamma_{qp}^{db,rs} \tag{14}$$

where the superscripts 'sr' and 'rs' stand for term (i) and term (ii) of the double bounce scattering, respectively.

For $\gamma_{qp}^{db,sr}$ (scattered by the scatterer and then reflected), we have

$$S_{pq}^{db,sr} = \sum_{j=1}^{N} R_p(\theta_s) \exp(2ik_{spz}d) \exp\left(-i\left(\overline{K}_{sp} - \overline{K}_{iq}\right) \cdot \overline{r}_j\right) f_{pq}(\pi - \theta_s, \phi_s; \pi - \theta_i, \phi_i) \tag{15}$$

where R_p is the coherent reflectivity of the rough surface for p polarization calculated from NMM3D [28], and d is the thickness of the vegetation layer.

Similarly, the assumption that the scatterers are statistically identical, mutually independent and uniformly distributed in the vegetation layer [8] leads to

$$\left\langle S_{pq}^{db,sr} S_{pq}^{db,sr*} \right\rangle = \mathrm{n}_0 A \int_{-d}^{0} dz_j \left\{ \begin{array}{l} \exp(2\mathrm{Im}(-k_{spz} + k_{iqz}) z_j) |R_p(\theta_s)|^2 \times \\ \exp(-4\mathrm{Im}(k_{spz}) d) \left\langle |f_{pq}(\pi - \theta_s, \phi_s; \pi - \theta_i, \phi_i)|^2 \right\rangle \end{array} \right\} \tag{16}$$

After simplification and substituting into Equation (5), we obtain

$$\gamma_{pq}^{db,sr} = \begin{cases} \left[\begin{array}{l} \dfrac{4\pi n_0}{\cos\theta_i} \dfrac{1 - \exp(2(\mathrm{Im}(k_{spz}) - \mathrm{Im}(k_{iqz}))d)}{2(-\mathrm{Im}(k_{spz}) + \mathrm{Im}(k_{iqz}))} \\ \times |R_p(\theta_s)|^2 \exp(-4\mathrm{Im}(k_{spz}) d) \left\langle |f_{pq}(\pi - \theta_s, \phi_s; \pi - \theta_i, \phi_i)|^2 \right\rangle \end{array} \right] & \text{if } \mathrm{Im}(k_{spz}) \neq \mathrm{Im}(k_{iqz}) \\ \dfrac{4\pi n_0 d}{\cos\theta_i} |R_p(\theta_s)|^2 \exp(-4\mathrm{Im}(k_{spz}) d) \left\langle |f_{pq}(\pi - \theta_s, \phi_s; \pi - \theta_i, \phi_i)|^2 \right\rangle & \text{if } \mathrm{Im}(k_{spz}) = \mathrm{Im}(k_{iqz}) \end{cases} \tag{17}$$

For the other term in the double bounce scattering, $\gamma_{qp}^{db,sr}$ (reflected by the rough surface and then scattered by the scatterer),

$$S_{pq}^{db,rs} = \sum_{j=1}^{N} R_q(\theta_i) \exp(2ik_{iqz}d) \exp\left(-i\left(\overline{k}_{sp} - \overline{k}_{iq}\right) \cdot \overline{r}_j\right) f_{pq}(\theta_s, \phi_s; \theta_i, \phi_i) \tag{18}$$

Similarly, assuming independent scattering and that the scatterers are statistically identical and uniformly distributed in the vegetation layer [8],

$$\left\langle S_{pq}^{db,rs} S_{pq}^{db,rs*} \right\rangle = \mathrm{n}_0 A \int_{-d}^{0} dz_j \left\{ \begin{array}{l} \exp(2\mathrm{Im}(k_{spz} - k_{iqz}) z_j) |R_q(\theta_i)|^2 \\ \times \exp(-4\mathrm{Im}(k_{iqz}) d) \left\langle |f_{pq}(\theta_s, \phi_s; \theta_i, \phi_i)|^2 \right\rangle \end{array} \right\} \tag{19}$$

Finally, $\gamma_{pq}^{db,sr}$ can be expressed as:

$$\gamma_{pq}^{db,sr} = \begin{cases} \left[\begin{array}{l} \dfrac{4\pi n_0}{\cos\theta_i} \dfrac{1 - \exp(-2(\mathrm{Im}(k_{spz}) - \mathrm{Im}(k_{iqz}))d)}{2(\mathrm{Im}(k_{spz}) - \mathrm{Im}(k_{iqz}))} \\ \times |R_q(\theta_i)|^2 \exp(-4\mathrm{Im}(k_{iqz}) d) \left\langle |f_{pq}(\theta_s, \phi_s; \theta_i, \phi_i)|^2 \right\rangle \end{array} \right] & \text{if } \mathrm{Im}(k_{spz}) \neq \mathrm{Im}(k_{iqz}) \\ \dfrac{4\pi n_0 d}{\cos\theta_i} |R_q(\theta_i)|^2 \exp(-4\mathrm{Im}(k_{iqz}) d) \left\langle |f_{pq}(\theta_s, \phi_s; \theta_i, \phi_i)|^2 \right\rangle & \text{if } \mathrm{Im}(k_{spz}) = \mathrm{Im}(k_{iqz}) \end{cases} \tag{20}$$

Finally, for surface scattering, the bistatic scattering can be expressed as [11, 13]:

$$S_{pq}^{surf} = \exp(ik_{spz}d) \exp(ik_{iqz}d) S_{pq}^{R} \tag{21}$$

where S_{pq}^{R} is the surface scattering of bare soil calculated from NMM3D [11] and the exponential parts account for the attenuation through the vegetation layer.

In NMM3D, Maxwell equations are solved numerically based on MoM and RWG basis functions, which is an intensive computational problem [28]. Tapered incidence fields are used since the simulated random rough surface is of finite extent, and the results for infinite surfaces are extracted from the simulations of the finite surfaces [28]. The soil surfaces are assumed to be Gaussian random rough surfaces with exponential correlation functions, which appear to provide the best fit to the natural surfaces among the correlation functions reported in literature [4]. For L-band in this paper, the surface area used for simulations in NMM3D is 16 by 16 square wavelengths. In this case, the RMS heights that can be simulated are within the range of $0 \sim 5\,\mathrm{cm}$ (0.21 wavelengths) which covers the RMS heights

for all the fields studied in this paper and captures the wide range of the natural conditions [13]. If an RMS height larger than 0.21 wavelengths is required, a larger surface area has to be simulated, which requires more computation resources and time.

Then, γ_{pq}^{surf} can be calculated by substituting the following expression into Equation (17).

$$\left\langle S_{pq}^{surf} S_{pq}^{surf*} \right\rangle = \exp\left(-2\mathrm{Im}\left(k_{spz}\right) d\right) \exp\left(-2\mathrm{Im}\left(k_{iqz}\right) d\right) \left\langle S_{pq}^{R} S_{pq}^{R*} \right\rangle \tag{22}$$

After calculating the bistatic scattering coefficients γ, the emissivity is obtained by the integration of γ over the hemispherical solid angle as shown in Equation (1). Finally, multiplying the emissivity by the physical temperature yields the brightness temperature of the vegetation fields.

For active microwave remote sensing, the backscattering coefficients are needed. We used the same vegetation model and formulations as illustrated above to calculate the backscattering coefficients and substitute $\theta_s = \theta_i$ and $\phi_s = \phi_i + \pi$ which indicate the backscattering direction into the equations. In this way, the active and passive models are founded on the same theoretical basis and the same physical parameters as will be explained in Section 3 are used.

In comparison, the formulas for the tau-omega model which only computes the brightness temperature instead of the backscattering coefficient are also presented here. In the tau-omega model [29], the brightness temperature T_B of the vegetated surface is calculated as:

$$\begin{aligned} T_B\left(\theta\right) \;=\; & T_{soil}\left(1 - r\left(\theta\right)\right) \exp\left(-\tau \cdot \sec\left(\theta\right)\right) \\ & + T_{veg}\left(1 - \omega\right)\left(1 - \exp\left(-\tau \cdot \sec\left(\theta\right)\right)\right)\left(1 + r\left(\theta\right) \cdot \exp\left(-\tau \cdot \sec\left(\theta\right)\right)\right) \end{aligned} \tag{23}$$

where θ is the observation angle of 40 degrees for SMAP and PALS in SMAPVEX12, T_{soil} is the physical temperature of the soil, T_{veg} is the physical temperature of the vegetation, ω is the scattering albedo of the vegetation, $\tau = b \times VWC$ is the vegetation optical thickness and $r(\theta)$ is the reflectivity of the soil surface defined as [29, 30]:

$$r_p\left(\theta\right) = \left(\left(1 - Q\right) r_{0,p} + Q r_{0,q}\right) \exp\left(-h\cos^2\left(\theta\right)\right) \tag{24}$$

where the subscripts 'p' and 'q' denote polarization, r_0 is the reflectivity of the smooth surface calculated from the Fresnel equations, Q is the polarization mixing coefficient, and h is the effective roughness parameter defined as [30]:

$$h = \left(2\sigma k_0\right)^2 \tag{25}$$

where σ is the RMS height of the soil surface and k_0 is the wave number in free space.

The tau-omega model for passive microwaves uses empirical parameters instead of physical parameters and is totally different from the NMM3D-DBA model used for active microwaves. On the other hand, the combined active and passive model derived in the paper uses the same model NMM3D-DBA and the same input physical parameters for both active and passive microwaves.

3. AIRBORNE AND FIELD CAMPAIGN DATA FROM SMAPVEX12

3.1. SMAPVEX12 Campaign Overview

To validate the consistent combined active and passive model NMM3D-DBA, we used the measurement data from the SMAPVEX12 campaign. The SMAPVEX12 campaign is briefly summarized in this section and its details are available in [14]. As described in [14], SMAPVEX12 was a field campaign designed to support the development and assessment of SMAP soil moisture products in an agricultural area of approximately 15 km × 70 km located within the larger Red River Watershed south of Winnipeg, Manitoba (Canada). SMAPVEX12 was conducted between June 7 and July 19, 2012 during which soil moisture and vegetation conditions varied significantly. The campaign provided extended-duration measurements exceeding the duration of any past soil moisture remote sensing field experiments. The study area of SMAPVEX12 is shown in Figure 6, where the dominant vegetation types are cereals (including wheat, winter wheat and oat), soybeans, canola, corn and pasture. The number of soybean fields is largest among all the sampling fields, as compared to the other vegetation types. The SMAPVEX12 campaign provided vegetation data, soil moisture data and coincident backscatterer and brightness temperature data which are of value in algorithm development for vegetated surfaces.

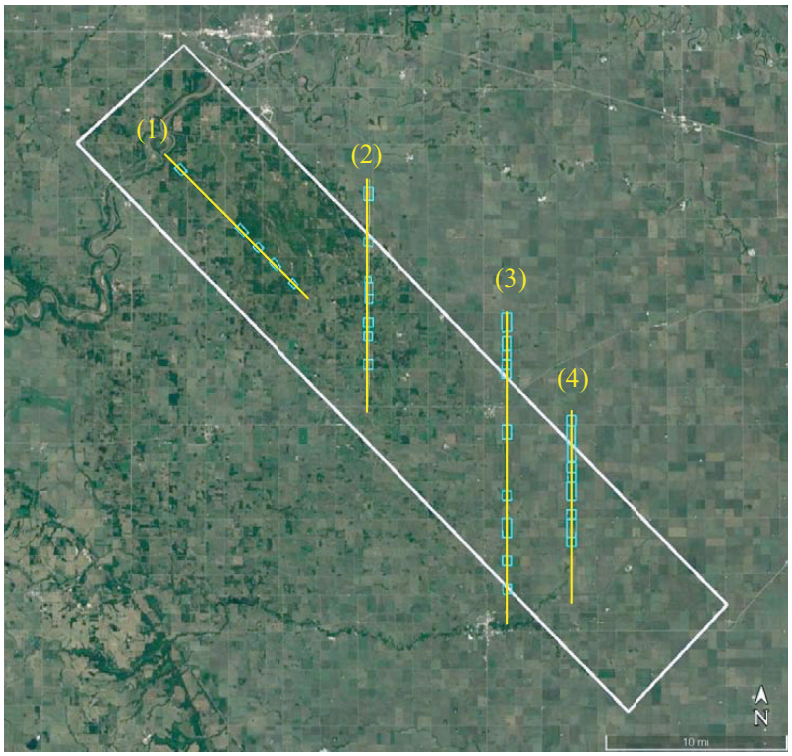

Figure 6. SMAPVEX12 study area (white box), sampling fields (cyan boxes) and low altitude PALS flight lines (yellow lines).

Flights of the UAVSAR [31], an aircraft-based fully polarimetric L-band radar, provided backscatter data of high-quality from its stable platform with high spatial resolution and reliable calibration. For UAVSAR, the noise floor was −45 dB and the relative calibration error was 0.3 dB. Flights of the PALS provided both brightness temperature and radar backscatter data. For the passive sensor of PALS, the noise level for the field averages was less than 0.1 K and the calibration accuracy was 0.2 K. The UAVSAR was flown on a G-III aircraft while the PALS was flown on a Twin Otter. The flight lines of low altitude PALS are shown in Figure 6 where the lines (3) and (4) were also flown by UAVSAR. Both aircrafts were flown several times per week providing coverage with a temporal frequency similar to that of the SMAP satellite. The operating frequencies were 1.413 GHz and 1.26 GHz for PALS and UAVSAR, respectively. Data within the UAVSAR swath were collected over a wide range of incidence angles. These values were normalized to an incidence angle of 40 degrees using the histogram-matching method [32], in order to be comparable to the SMAP data. The residual error in the normalization is smaller than 1 dB standard deviation. Speckle noise was significantly removed by averaging single-look data at ~ 7 m resolution over each field ($\sim 800\,\text{m} \times 800\,\text{m}$). PALS was designed to measure data at a 40 degrees incidence angle, therefore, already matching the observation angle of SMAP. PALS data were acquired at both low and high aircraft altitudes. The low-altitude flights provided an effective resolution of 600 m, which is smaller than the typical field size of $\sim 800\,\text{m} \times 800\,\text{m}$. The PALS low-altitude data are hence more suitable for NMM3D-DBA model validation, which assumes homogeneous vegetation conditions. The PALS radiometer operates using a two-reference switching scheme with a matched load and a noise diode as the two references to remove internal gain fluctuations [33]. The calibration utilizes three measurements: the noise diode level, a lake and 45 degrees polarization rotation angle over the lake and land surface as detailed in [33]. The measured backscatter and brightness temperature data are compared with computed outputs from the model which will be illustrated in the following sections.

Other measured model inputs were *VWC*, *RMS* rough surface height, soil moisture, and soil and vegetation temperatures. *VWC* was measured through destructive sampling at three sample points within each sampling field by cutting and collecting the plants on the ground in a small area with all

the measurements scaled to 1 m^2 area. The water content is the wet weight minus dry weight obtained by drying the sampled plants in an oven for several days, then multiplied by a conversion factor to account for the little remaining water after the drying process. One of the error sources for the *VWC* measurement is the loss of the vegetation water during transportation of the plants from the fields to the weighting station to weigh their wet weight. In general, the quality of the SMAPVEX12 *VWC* data meets the typical expectation for this type of field campaign. The *RMS* height of each field is assumed to be constant during SMAPVEX12 since the experiment began after seeding without further tillage operations to affect the roughness. Furthermore, the vegetation canopy reduced the effect of erosion. The topography was approximately flat for the vegetation fields. The *RMS* surface roughness height of the field was acquired by post-processing measurements from a 1 m-long pin profilometer and digital camera. Repeated measurements were performed to obtain a 3 m profile consisting of three 1m profiles for each site. One of the error sources for the *RMS* height measurements is the human error in placing the profilometer in the fields. Even through it is difficult to validate the measured *RMS* height, the measurement method is generally used in similar soil moisture field experiments and should provide *RMS* height data with a typical quality standard. According to [34], the measurement uncertainty of the pin profilometer was about 2 mm in height based on a laboratory rainfall simulator study. On flight days, the fast-changing soil moisture was measured concurrently with the airborne acquisitions such that the backscatter and soil moisture data collection were near coincident. Handheld Stevens Water Hydra Probes connected to a Personal Digital Assistant were used to measure the surface soil moisture with site-specific calibrations [35, 36]; individual calibration equations were developed for each of the fields. The volumetric soil moisture measurements apply a default soil dielectric conversion model causing errors within 3%, which are further reduced by the site-specific calibration. There were 16 soil moisture sample points for each field with three replicate volumetric soil moisture measurements at each point to capture the spatial variability. Subsurface soil, surface soil and vegetation temperatures were also measured on flight days at four sites in each field. Subsurface soil temperatures were measured at 5 cm and 10 cm using a digital thermometer. The temperatures for sunlit and shaded vegetation and surface soil were recorded using a thermal infrared thermometer.

Vegetation attributes including crop density, plant height, stem diameter, stalk height, stalk angle, leaf thickness and leaf width were also measured. These observations provided a basis for choosing the parameters for the combined active and passive model. For each field, the plant density was obtained by counting the number of plants in ten rows with a 1m row length. Plant height and stem diameter were measured at the sample points for *VWC* just before cutting the vegetation samples with ten measurements at each point. The other vegetation attributes were measured at four wheat fields and three canola fields five to six times during the campaign [14]. For the SMAPVEX12 wheat and winter wheat fields, most of the data were taken during the stem elongation, booting, heading, and ripened stages. The pasture fields varied little throughout the campaign. The growth stages of the SMAPVEX12 canola crops progressed from leaf development to stem elongation and finally entering ripening.

3.2. Physical Parameters for Different Vegetation Types

To validate the combined active and passive model using SMAPVEX12 data the measured *RMS* height, *VWC* and in situ soil moisture are input to the model to compute backscatter and brightness temperature; these are then compared with the UAVSAR and PALS low-altitude radiometer measurements. Other physical parameters needed in the model including crop density, plant height, stalk orientation and leaf radius are derived from the ground measurements which are explained in detail for each vegetation type as below. In general, the measured data directly ingested into the model are the *RMS* height, *VWC* and in situ soil moisture. (The measured soil and vegetation temperatures are also directly given to the model to convert the emissivity to brightness temperature.) The other inputs are either constants estimated from field measurements or values calculated from the *VWC*, depending on how much the parameters changed during the SMAPVEX12 campaign. The goal of developing the forward models is to retrieve information about the vegetated surfaces, such as the soil moisture and *VWC*, from the radar and radiometer data. In the future, we plan to implement a data-cube retrieval algorithm as detailed in [13], where lookup tables are computed using the forward model with the three axes of *RMS* height, *VWC*, and soil moisture.

3.2.1. Wheat and Winter Wheat

Wheat is modeled as a layer of uniformly distributed cylinders with different orientations. For simplicity, the wheat leaves and ears are ignored since the wheat plants during SMPAVEX 12 were dominated by the stalks, as shown in Figure 3. The model parameters (diameter, density and orientations of the cylinders) for the wheat and winter wheat fields are presented in Table 1. The length of the cylinders is calculated from VWC using:

$$l = \frac{VWC}{\pi a^2 \rho_{water} n_a M veg_{wheat}} \tag{26}$$

where l, a, ρ_{water}, n_a and M_{veg} stand for length, radius, water density, number of cylinders per m^2 and volumetric water content of vegetation, respectively. The measured length is not used because it was not measured on flight days; instead, VWC was synchronized with the UAVSAR and PALS data. VWC measures the weight of the water contained in the vegetation in an area of $1\,\mathrm{m}^2$ which has the unit $\mathrm{kg/m}^2$. M_{veg} is defined as the volume of the water in plant divided by the total volume of the plant. M_{veg} is estimated from the gravimetric water content (M_g) measured during SMAPVEX12, which determines the dielectric constant [37] of leaves and stalks and subsequently affects the scattering by the vegetation.

Table 1. Physical parameters for the wheat fields. M_{veg} is the volumetric water content of the wheat. n_a is the number of wheat plants in $1\,\mathrm{m}^2$. β and α which define the orientation of the scatterer are the elevation angle and the azimuth angle, respectively, as shown in Figure 2. The probability function for the scatterer elevation angle is chosen to be $p(\beta) = C\sin^8(\beta)\cos^2(\beta)$ to achieve a good agreement between the data-cube and measurements. The coefficient C is determined so that the integration of $p(\beta)$ over $5^\circ \sim 30^\circ$ is 1. The distribution of the scatterer azimuth angle is uniform over all the angles. For winter wheat, M_{veg} is 70% and n_a is $450\,\mathrm{m}^{-2}$.

Diameter (mm)	M_{veg}	$n_a\,(m^{-2})$	β	α
2.6	80%	400	$5^\circ \sim 30^\circ$	$0 \sim 360^\circ$

3.2.2. Pasture

Pasture vegetation is modeled as a layer of uniformly distributed cylinders. The physical parameters (diameter, length and orientations of the cylinders) for the pasture field are presented in Table 2. The number of cylinders per unit volume is related to VWC:

$$n_0 = \frac{VWC}{\pi a^2 l^2 \rho_{water} M veg_{wheat}} \tag{27}$$

Table 2. Physical parameters for the pasture field. M_{veg} is the volumetric water content of the pasture. The probability function for the scatterer elevation angle (β, measured from vertical, as shown in Figure 2) is chosen to be $p(\beta) = C\sin^6(\beta)\cos(\beta)$ to achieve a good agreement between the data-cube and measurements. The coefficient C is determined so that the integration of $p(\beta)$ over $10 \sim 90^\circ$ is 1. The distribution of the scatterer azimuth angle (α as shown in Figure 2) is uniform over all the angles.

Diameter (mm)	M_{veg}	Length (cm)	β	α
3.0	80%	60	$10^\circ \sim 90^\circ$	$0 \sim 360^\circ$

3.2.3. Canola

For canola, two different kinds of cylinders with different radii and lengths are used to model its main stem and branches while circular disks are used to model its leaves, as shown in Figure 5(a). The leaf thickness is much smaller than the wavelength at L-band, and thus the total area of the leave

Table 3. Physical parameters for the canola fields. The values in parentheses are used starting from July 10th according to the data. The volumetric water content M_{veg} is estimated from the measured M_g in the same way as for the wheat [37]. VWC is measured in situ. d and l are derived from VWC based on the empirical allometric relationships. β is the scatterer elevation angle. The distribution of the azimuthal angle (α as shown in Figure 5(a)) is uniform over $0 \sim 360°$ for the stem, branch and leaves.

	Diameter (mm)	Length (cm)	M_{veg}	Distribution of β
Stem	d	l	60% (*40%*)	Uniform over $0 \sim 5°$
Branch	$d/2$	$l/3$	60% (*40%*)	Uniform over $0 \sim 50°$
Leaf	140 (*80*)	0.03	60% (*40%*)	Uniform over $70° \sim 90°$

is more important than its shape [26]. Similar to the pasture and wheat case, these elements are assumed to be uniformly distributed in the canola layer with different orientations. It can be seen from Figures 5(b) and (c) that the geometry of the canola plant in June was different from that in July. There were more leaves with larger radii in June than July. Thus, two sets of physical parameters were used for canola to represent the geometry of the canola plants at the respective growth stages. The parameters are listed in Table 3. The M_{veg} and leaf radius are adjusted to smaller values for the July data-cube based on the ground measurement data. It can be seen from Figures 5(b) and (c) that the canola in July appears to be withered compared to the conditions in June. From the in situ measurements, the average number of canola plants per m^2 (n_a) is about 60 and the number of leaves per plant (N_l) is about b ($b = 2$ for June and 1 for July, respectively) multiplied by the number of branches per plant (N_s). The main stem diameter (d) which increases with VWC is calculated from the allometric relationship with VWC obtained from the measurement data through curve fitting: $d = -0.03135VWC^2 + 0.938VWC + 4.87$ in mm, as shown in Figure 7(a). Similarly, the main stem length (l) is obtained as: $l = -121.4VWC^{-1.186} + 130.2$ in cm, as shown in Figure 7(b). N_s can be calculated from VWC using the following formula:

$$N_s = \frac{VWC - \rho_{water} n_a Vol_{stem} Mveg_{stem}}{n_a \rho_{water} (Vol_{branch} Mveg_{branch} + b\, Vol_{leaf} Mveg_{leaf})} \tag{28}$$

where Vol_{stem}, Vol_{branch} and Vol_{leaf} are the volume of stem, branch and leaf, respectively.

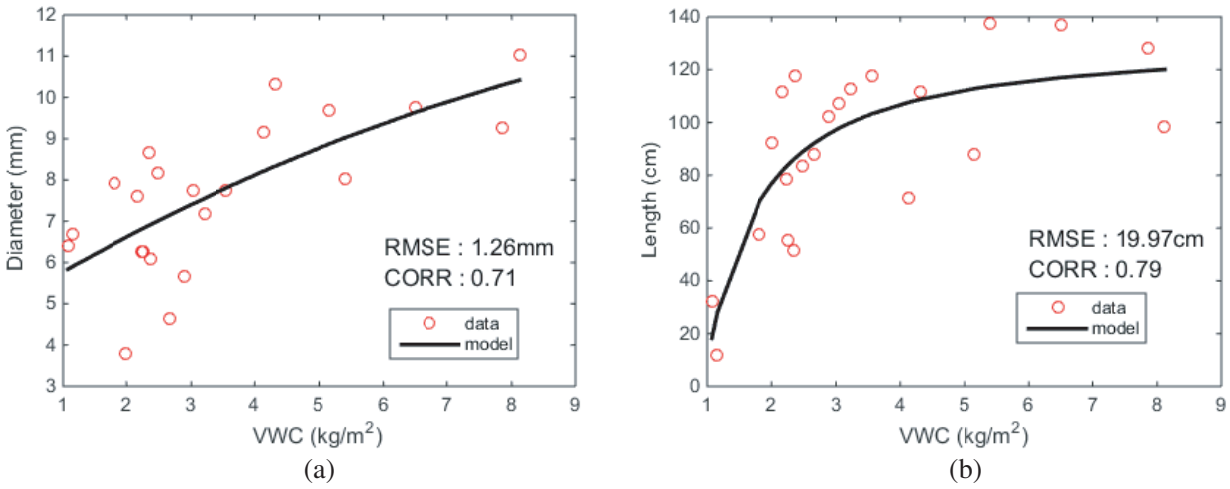

Figure 7. Vegetation parameters for canola during SMAPVEX12: (a) main stem diameter as a function of VWC, (b) main stem length as a function of VWC.

4. MODEL VALIDATION FOR VEGETATION TYPES

The measured *RMS* height, *VWC*, in situ soil moisture, and soil and vegetation temperature, as well as the physical parameters presented in Section 3.2 are used as inputs to the combined active and passive model, as summarized in Table 4. The calculated backscatter coefficients and brightness temperatures are validated using concurrent airborne PALS low-altitude radiometer data and UAVSAR data for each day of flights during the SMAPVEX12 field campaign. The radar measurements from UAVSAR are used because they provide higher spatial resolution than PALS. Only fields that have PALS low-altitude radiometer data are considered here because the focus in this paper is on the joint validation of emissivity and backscatter calculated from the combined active and passive model. The time-series forward comparison between the model results and measurement data for the wheat fields is presented in Figures 8, 9(a) and (b), and 10(a), where (a) shows brightness temperature while (b) shows backscatter. Since there are no UAVSAR data to compare for field 931, therefore only brightness temperature comparisons are presented in Figure 10(a). For the three wheat fields, the same set of vegetation parameters (such as radius, orientation and crop density) are used to characterize the vegetation but

Table 4. Input parameters for the combined active and passive model. The parameters indicated with '*' are estimated from measurements whose values are listed in Tables 1 $\sim$ 3. The parameters indicated with '**' are calculated from measured *VWC*, where the formulas are presented in Section 3.2. The remaining parameters without any indicators are directly ingested in the model with their measured values. The orientation is defined by the probability function of the two orientation angles α and β.

Land Cover	Input Parameters for the Combined Active and Passive Model
wheat/ winter wheat	*VWC*, *RMS* rough surface height, soil moisture, soil and vegetation temperatures, diameter*, M_{veg}*, length**, n_a*, orientation*
pasture	*VWC*, *RMS* rough surface height, soil moisture, soil and vegetation temperatures, diameter*, M_{veg}*, length*, n_0**, orientation*
canola	*VWC*, *RMS* rough surface height, soil moisture, soil and vegetation temperatures, n_a*, stem diameter**, stem M_{veg}*, stem length**, stem orientation*, stalk diameter**, stalk M_{veg}*, stalk length**, stalk orientation*, leaf diameter*, leaf M_{veg}*, leaf thickness*, leaf orientation*

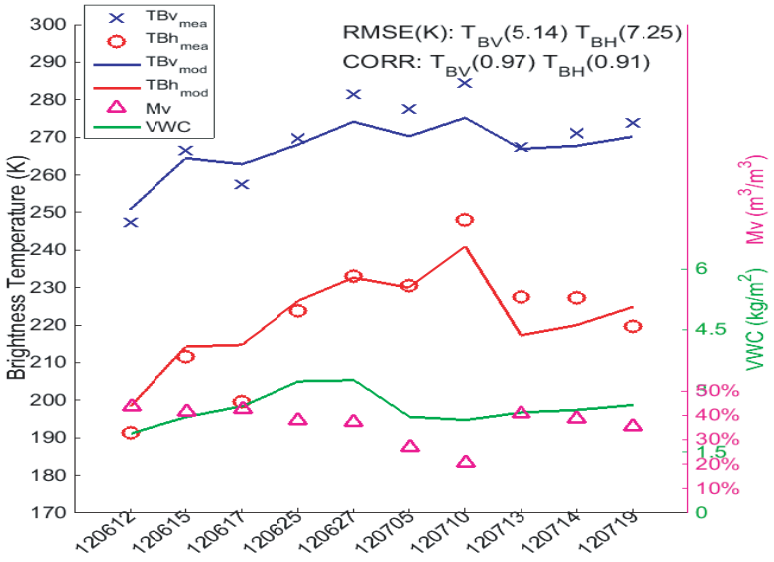

(a)

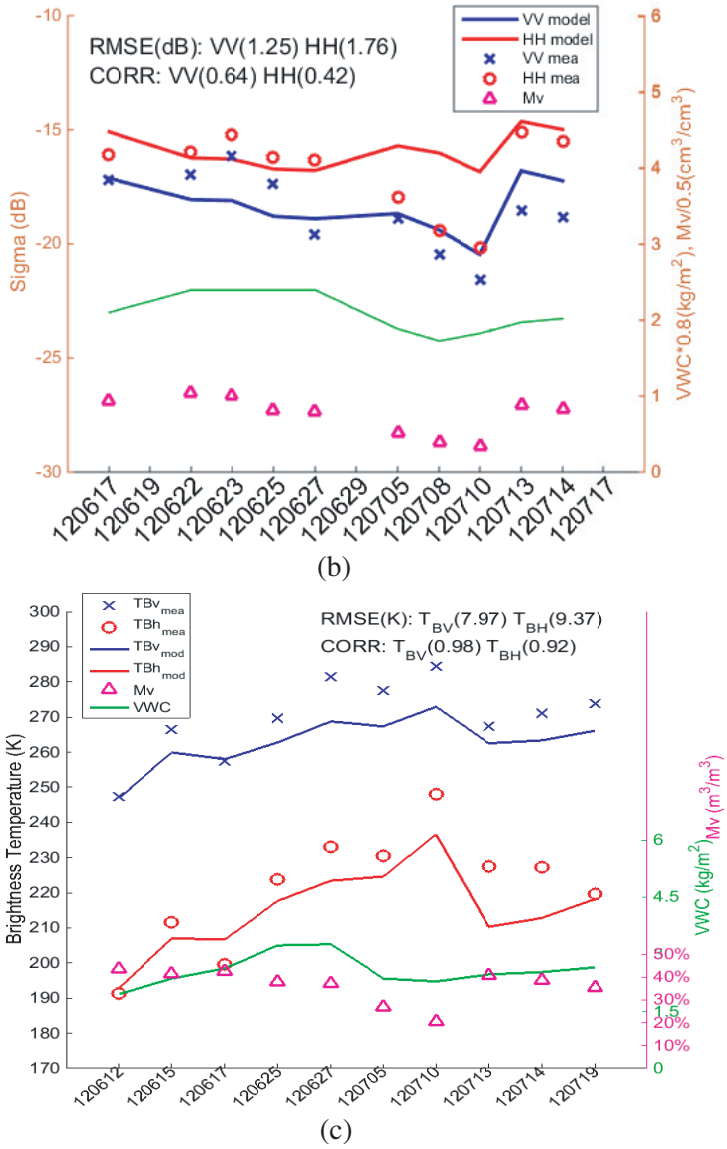

Figure 8. Model and measurement comparison of wheat field 31 for (a) brightness temperature using NMM3D-DBA, (b) backscatter using NMM3D-DBA, (c) brightness temperature using the tau-omega model. Soil surface RMS height is 0.81 cm. "CORR"stands for "correlation coefficient". "TBV$_{mea}$" and "TBH$_{mea}$" indicate measured brightness temperature at vertical polarization and horizontal polarization from the PALS radiometer. "TBV$_{mod}$" and "TBH$_{mod}$" represent the modeled brightness temperature at vertical polarization and horizontal polarization. "Mv"stands for soil moisture. "VV model" and "HH model" indicate modeled backscatter. "VV_{mea}" and "HH_{mea}" are measured backscatter from the UAVSAR. Soil moisture (Mv) and VWC are scaled as $Mv/0.5$ and $VWC * 0.8$ for the backscatter plot, respectively. The x-axis presents the campaign date. For example, "120615" represents June 15th, 2012. The same notations apply for Figures 6–12.

the measured RMS height, VWC, in situ soil moisture, and soil and vegetation temperature are different for the different fields. This is useful for the data-cube based soil moisture retrieval [13, 38] where a lookup table is inverted. This lookup table is computed using the forward model with the same set of parameters for each group of vegetation. It is worth mentioning that the input parameters and the allometric relationships from curve fitting based on the SMAPVEX12 ground measurements will put a burden on a future data-cube based inversion methodology where only three variables (RMS height,

VWC and soil moisture) can be retrieved. The root mean squared error (RMSE) between the modeled and measured backscatter is calculated using:

$$RMSE = \sqrt{\frac{1}{N}\sum_{i=1}^{N}(\sigma_{data,i} - \sigma_{model,i})^2} \tag{29}$$

where N is the number of samples, σ_{data} the measured backscattering coefficient and σ_{model} the predicted backscattering coefficient from the model.

The RMSE between the modeled and measured brightness temperature is calculated in the same way. In terms of the RMSE and correlation coefficients, the consistent combined and passive model NMM3D-DBA provides a good prediction for the wheat fields for both active and passive for both polarizations under various soil and vegetation conditions. It is observed that the model results agree better with the measurements for V-pol than H-pol for both backscatters and brightness temperatures. This may be caused by that we modelled the wheat canopy as a layer of cylinders where the wheat leaves were ignored, resulting in more errors in H-pol than V-pol. The wheat leaves were oriented nearly parallel to the ground, as shown in Figure 3, so that the horizontally polarized incident waves

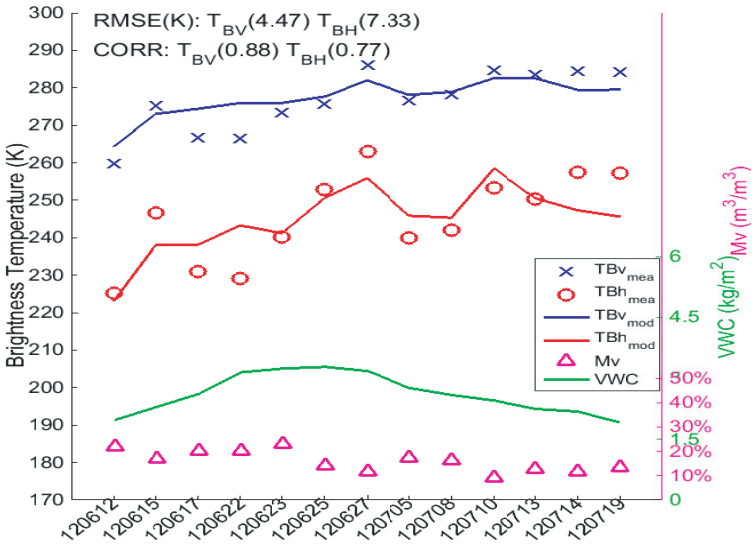

(a)

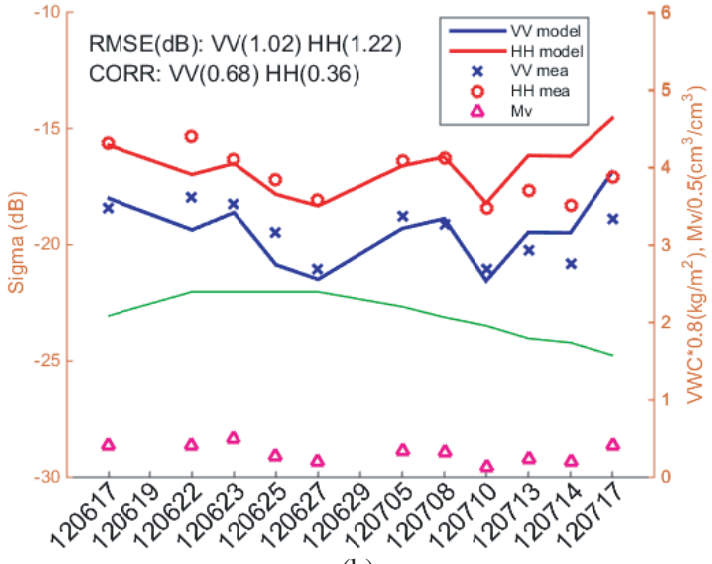

(b)

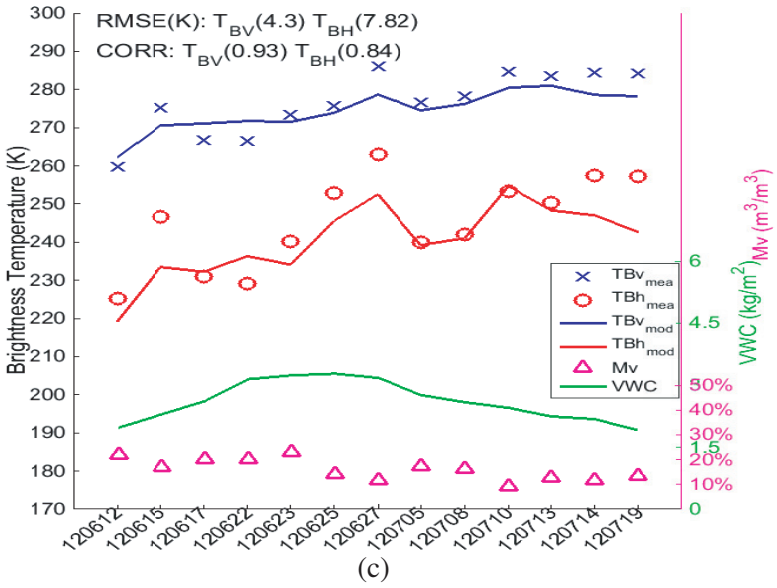

Figure 9. Model and measurement comparison of wheat field 91 for (a) brightness temperature using NMM3D-DBA, (b) backscatter using NMM3D-DBA, (c) brightness temperature using tau-omega model. Soil surface RMS height is 0.91 cm.

(H-pol) coupled more into the wheat leaves than the vertically polarized ones (V-pol). It is also observed that towards the end of the campaign, the NMM3D-DBA model generally overestimates the backscatter. This may be explained by the use of a fixed M_{veg} value for the whole period for simplicity and feasibility [13, 38]. As the wheat ripened, its M_{veg} generally decreased. Thus, during the end of the campaign, a higher M_{veg} value is used in the model, resulting in larger vegetation permittivity and larger scattering than expected. This general overestimation or underestimation in the last few campaign days is not observed in the brightness temperature comparisons. Similarly, the time-series forward comparisons for the winter wheat fields are presented in Figures 11, 12(a) and (b), and 13(a). There is no UAVSAR data to compare for field 941. It can be seen that the comparisons are similar to those of the wheat fields. The wheat and winter wheat were based on the same vegetation model and similar physical parameters were used.

For the pasture field, the comparison results are presented as time-series in Figures 14(a) and (b). The VWC of the pasture fields stays almost constant during the whole campaign period. It is observed from both the model results and measured radiometer and radar data that when the soil moisture increases with a fixed VWC, the brightness temperature generally decreases while the backscatter increases; and vice versa. This can be explained from the combined active and passive model as follows: when soil moisture increases, the soil permittivity increases. Then, the scattering from the soil surface and the soil surface reflectivity increase. For a fixed VWC, the attenuation through the vegetation layer and the vegetation scattering stay unchanged. Thus, the total scattering from the vegetated surface composed of surface scattering, double bounce scattering and volume scattering increases. Therefore, the backscatter increases while the brightness temperature proportional to the emissivity, which is one minus the integration of bistatic scattering, decreases. The changes of the VV and HH ratio, as well as the TBv (brightness temperature for V-pol) and TBh (brightness temperature for H-pol) ratio, with the soil moisture are also observed in both the model results and measurements. It is also noticed in Figure 14(b) that there are some mismatches for polarization ratio of VV and HH between model and measurements. This may be caused by the reason that a constant pasture orientation is used in the model but the pasture orientation could be changed by the wind and rain. The pasture orientation is hard to measure and the data of orientation for different dates is not available. The general polarization mismatch is not observed in the brightness temperature comparisons.

For the canola field, the comparison results are presented as time-series in Figures 15(a) and (b).

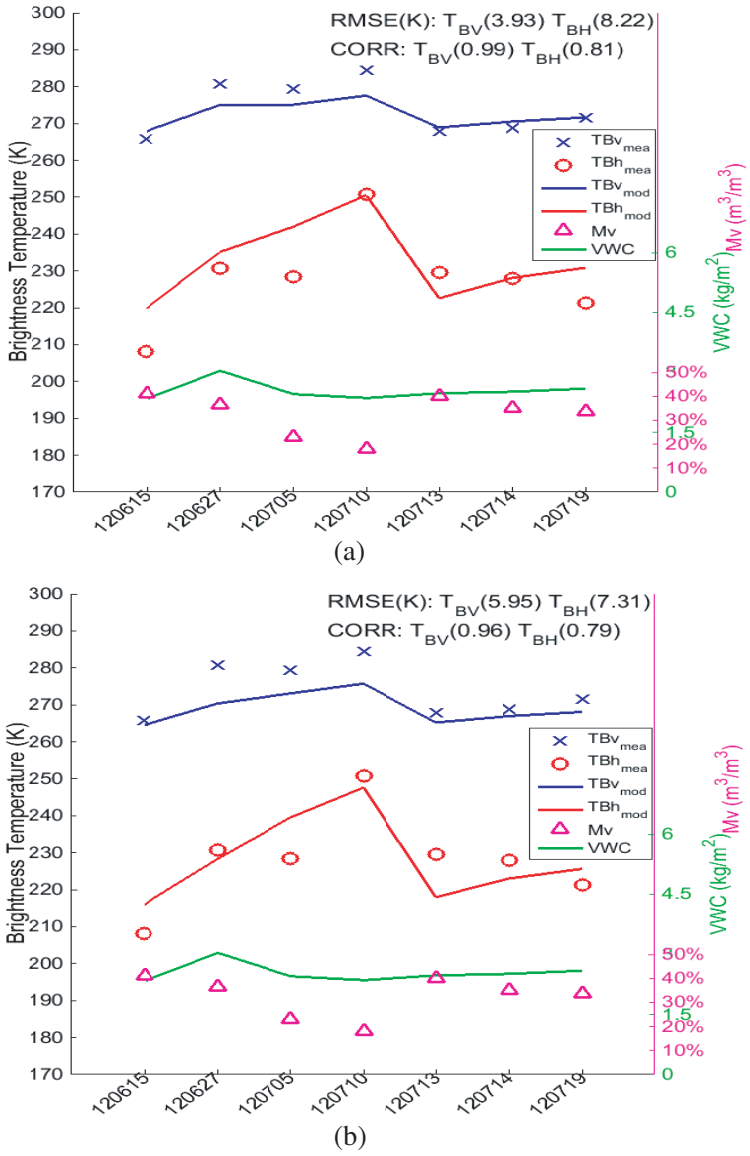

Figure 10. Model and measurement comparison of wheat field 931 for brightness temperature using (a) NMM3D-DBA, (b) tau-omega model. Soil surface RMS height is 1.00 cm.

From June 25th to June 27th, the soil moisture increased, but the measured brightness temperature increased and the backscatters decreased. This may be caused by the decrease of the *VWC* between these two days, which resulted in less attenuation for the surface scattering and less vegetation scattering. Mismatches between the model and measurements for brightness temperature are observed from June 25th to June 29th, which are larger than the other dates, especially for *H*-pol. However, this is not observed in the backscatter comparisons. This could be caused by the constant *RMS* height used during the whole period. The soil moisture was relatively low from June 25th to June 29th, and thus the surface scattering is relatively small compared with the volume scattering and double bounce scattering in the backscattering direction. Therefore, the error caused by *RMS* height which has the most influence on surface scattering does not affect the total backscatter much. On the other hand, the integration of surface scattering over the bistatic directions including the specular direction is also important compared with the integration of volume scattering and double bounce scattering. Thus the constant *RMS* height assumption in the model has a larger influence on the brightness temperature than the backscatter.

Table 5. RMSE and correlation coefficient (CORR) of backscatter and brightness temperatures (T_B) between model results and UAVSAR and PALS low-altitude radiometer observations. There is no UAVSAR data available for field 931 and 941 to compare with the modeled backscatter.

Field No.	Land Cover	Backscatter (NMM3D-DBA)				TB (NMM3D-DBA)				TB (Tau-omega)			
		RMSE (dB)		CORR		RMSE (K)		CORR		RMSE (K)		CORR	
		VV	HH	VV	HH	V	H	V	H	V	H	V	H
31	wheat	1.25	1.76	0.64	0.42	5.14	7.25	0.97	0.91	7.79	9.37	0.98	0.92
91		1.02	1.22	0.68	0.36	4.47	7.33	0.88	0.77	4.30	7.82	0.93	0.84
931		-	-	-	-	3.93	8.22	0.99	0.81	5.95	7.31	0.96	0.79
41	winter wheat	1.32	1.45	0.61	0.53	4.98	5.59	0.75	0.88	4.82	5.84	0.88	0.90
42		1.19	1.28	0.73	0.59	3.97	7.20	0.98	0.93	4.21	15.1	0.94	0.91
941		-	-	-	-	5.06	3.71	0.96	0.97	6.02	3.98	0.97	0.95
21	pasture	0.90	0.97	0.61	0.65	4.85	4.20	0.95	0.93	8.08	18.4	0.88	0.90
61	canola	0.66	0.79	0.94	0.98	4.09	6.98	0.91	0.90	3.68	8.93	0.90	0.83

In the NMM3D-DBA model the same input parameters are used to compute both brightness temperature and backscatter. In terms of the RMSE and correlation coefficient between the model and measurement, the modeled backscatters are in good agreement with the UAVSAR data, while the modeled brightness temperatures are in good agreement with the PALS low-altitude radiometer data. For vertical polarization, the averaged RMSE and correlation coefficient over all the fields are 4.65 K and 0.91 for brightness temperature and 1.04 dB and 0.95 for backscatter at VV, as shown in the scatter plots in Figure 16. For horizontal polarization, the average RMSE and correlation coefficient are 6.44 K and 0.94 for brightness temperature and 1.21 dB and 0.90 for backscatter at HH, as shown in Figure 17. According to the analysis above, the defects in the vegetation modelling such as ignoring the wheat leaves generally have more influence on the backscatter than the brightness temperature while the defects in the rough surface modelling such as using a constant RMS height generally have more influence on the brightness temperature than the backscatter, for the vegetation fields studied in this paper. The RMSE and correlation coefficient for each field are summarized in Table 5. Values in columns 3–6 are for the backscatter while columns 7–10 show values for brightness temperature. The

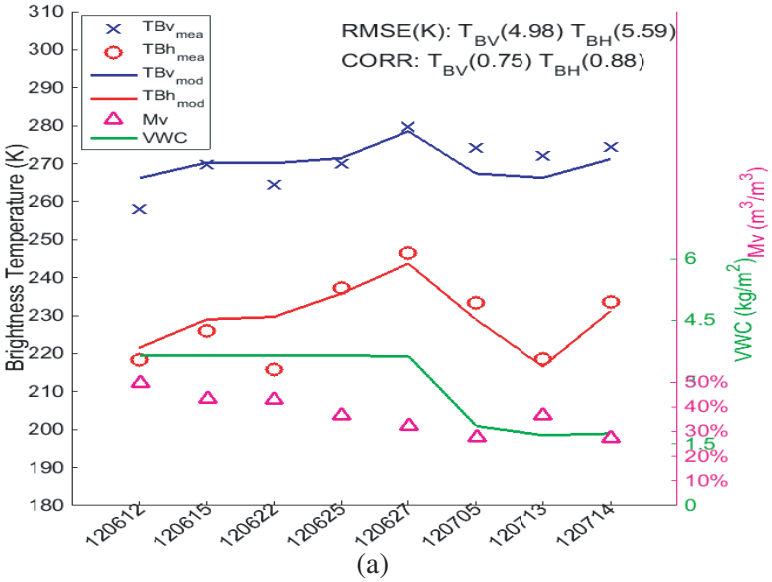

(a)

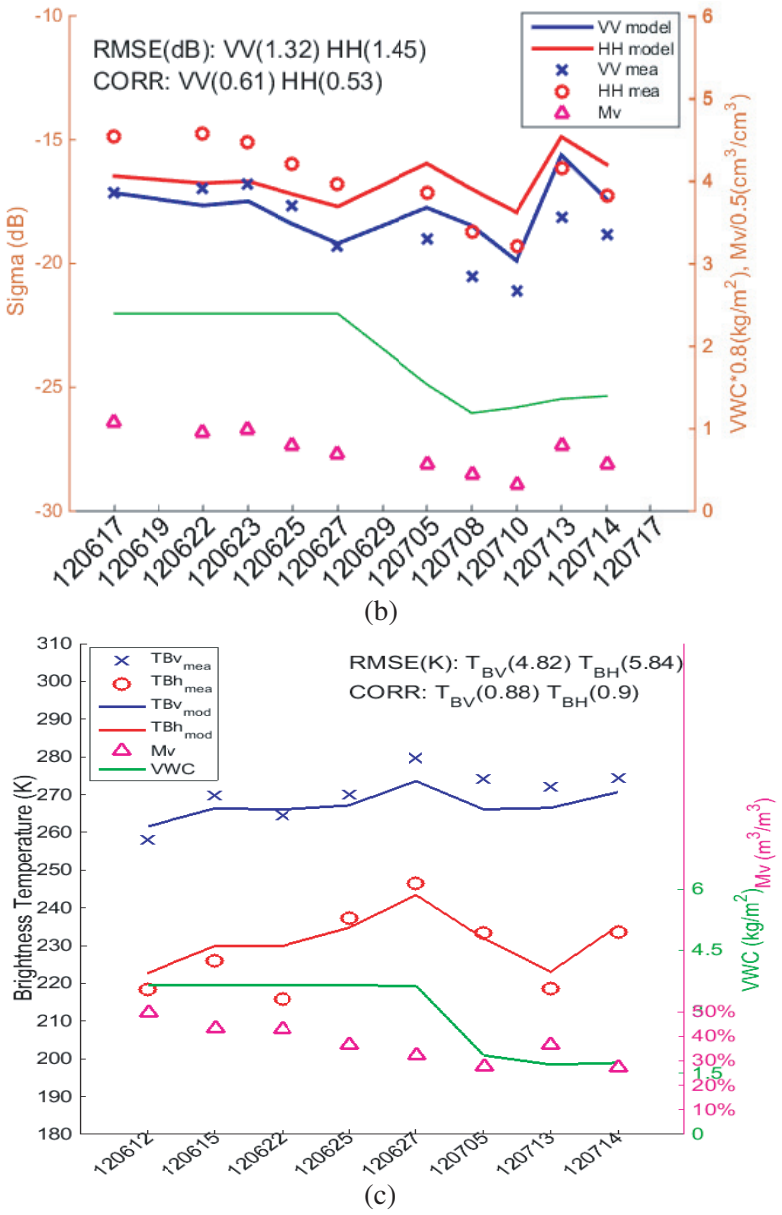

Figure 11. Model and measurement comparison of winter wheat field 41 for (a) brightness temperature using NMM3D-DBA, (b) backscatter using NMM3D-DBA, (c) brightness temperature using tau-omega model. Soil surface RMS height is 1.15 cm.

values in the last four columns are the results from the tau-omega model, which will be explained in the following section.

The sources of error, when comparing the backscatters from NMM3D-DBA and the measurement data, are detailed in [13]. Thus, we focus on analyzing the sources of error between the brightness temperature computed from NMM3D-DBA and the measured values from the low altitude PALS. One of the main sources of error is expected to come from the measurement error in *RMS* rough surface height. The contribution from the bistatic surface scattering generally dominates among the three scattering mechanisms for the wheat, winter wheat, pasture and canola fields studied in this paper. The surface scattering strongly depends on the *RMS* height. Thus, the emissivity and brightness temperature also strongly depend on the *RMS* height. Furthermore, there is considerable uncertainty in the roughness measurements [21]. The *RMS* height was measured only once and thus a constant *RMS* height was

used for the whole study period for each field [14]. The *RMS* height could have been influenced by rain, which would flatten the soil surface. Furthermore, the *RMS* height was measured at only two locations in each field, assuming the roughness variations are small over the same field [14] which may not be true. The change of brightness temperature with the *RMS* height for the bare soil surface computed from NMM3D-DBA is plotted in Figure 18 where a volumetric soil moisture of 25% m^3/m^3 and soil physical temperature of 25°C are used; these are around the average measured values of all the fields. The range of the *RMS* height in the figure covers the typical values for the vegetated surfaces at L-band. It can be seen from the figure that 0.1 cm change in *RMS* height results in brightness temperature change of about 1 K and 2 K for *V*-pol and *H*-pol, respectively. Some other sources of error to be considered when interpreting the results are: (1) the spatial variations of the soil moisture and VWC are not considered; (2) UAVSAR data, more specifically the normalization error when transforming the raw data to 40° (RMSE is about 1 dB [14]); (3) PALS data and the associated calibration error as detailed in [33]; (4) the physical temperature used to calculate brightness temperature from emissivity. The physical temperature of the soil-vegetation continuum is necessary to precisely calculate the brightness temperature from the emissivity [39]. Since it is not available, an averaged measured soil and vegetation

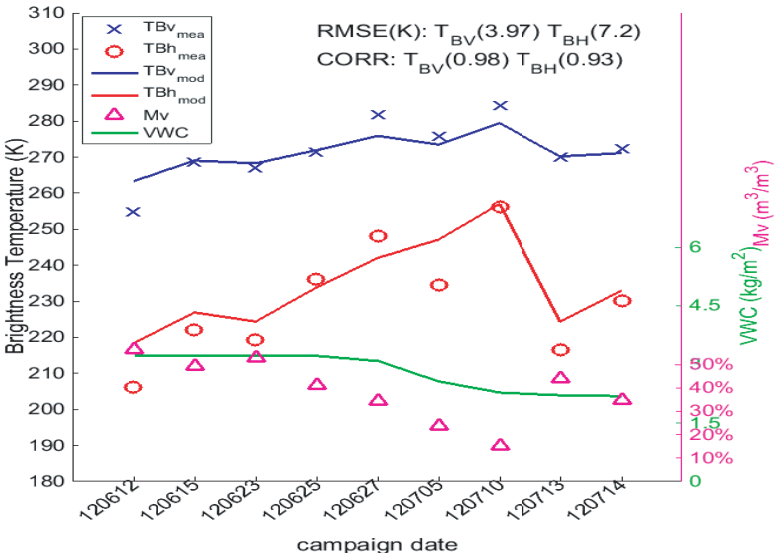

(a)

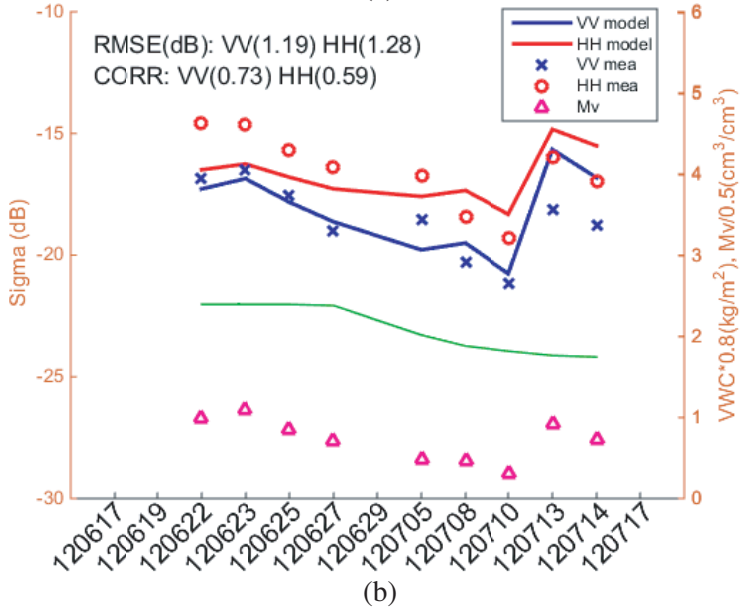

(b)

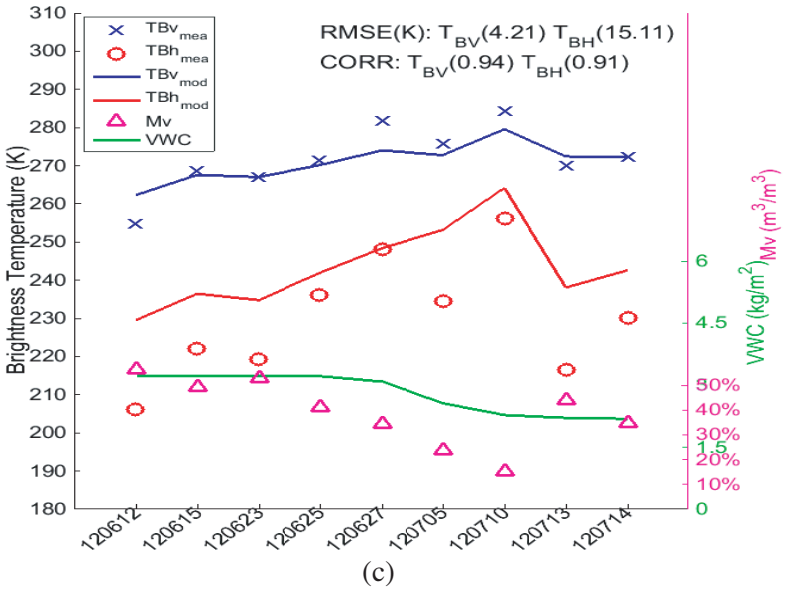

(c)

Figure 12. Model and measurement comparison of winter wheat field 42 for (a) brightness temperature using NMM3D-DBA, (b) backscatter using NMM3D-DBA, (c) brightness temperature using tau-omega model. Soil surface RMS height is 1.61 cm.

temperature is used instead; (5) model parameters. The plant geometry such as radius and length varies for different plants and average values are used; (6) NMM3D-DBA model. The scatterers are assumed to be uniformly distributed in the vegetation layer, which is not strictly true for the crop fields; and (7) the resolution/scaling gap between model and observations. The model assumes vegetated field is homogeneous which is better applicable to small scales than large scales.

Table 6. Comparison of vegetation scattering parameter ω and vegetation parameter b used in the tau-omega model for SMAPVEX12 [30] and calculated (cal.) from the NMM3D-DBA model.

Land Cover	Tau-omega				NMM3D-DBA			
	ω_V	ω_H	b_V	b_H	cal. ω_V	cal. ω_H	cal. b_V	cal. b_H
wheat	0.05	0.05	0.20	0.08	0.33	0.27	0.24	0.08
w. wheat	0.05	0.05	0.20	0.08	0.27	0.21	0.21	0.07
pasture	0.05	0.05	0.10	0.10	0.41	0.41	0.25	0.23
canola	0.05	0.05	0.21	0.12	0.15	0.15	0.26	0.24

* "w. wheat" is short for 'winter wheat"

5. COMPARISONS WITH THE TAU-OMEGA MODEL

The tau-omega model is derived from the zeroth order solution of the radiative transfer equation. Since the zeroth order solution ignores the phase matrix term, it is only valid when ω is small. However, typical calculated values of ω at L-band are in the range of 0.15 to 0.41 using the physical scattering model of branches and leaves as shown in Table 6. The value of ω used to fit the tau-omega model to observations is thus an empirically-determined effective parameter rather than a physical parameter. The value of ω used in the tau-omega model for SMAPVEX12 was empirically set to 0.05 to best match the SMAPVEX12 PALS low-altitude radiometer data [30] to the tau-omega model and is much smaller than the physically calculated ω as shown in Table 6. The physically-based ω is defined as $\omega = \langle \kappa_s \rangle / \langle \kappa_e \rangle$ [8],

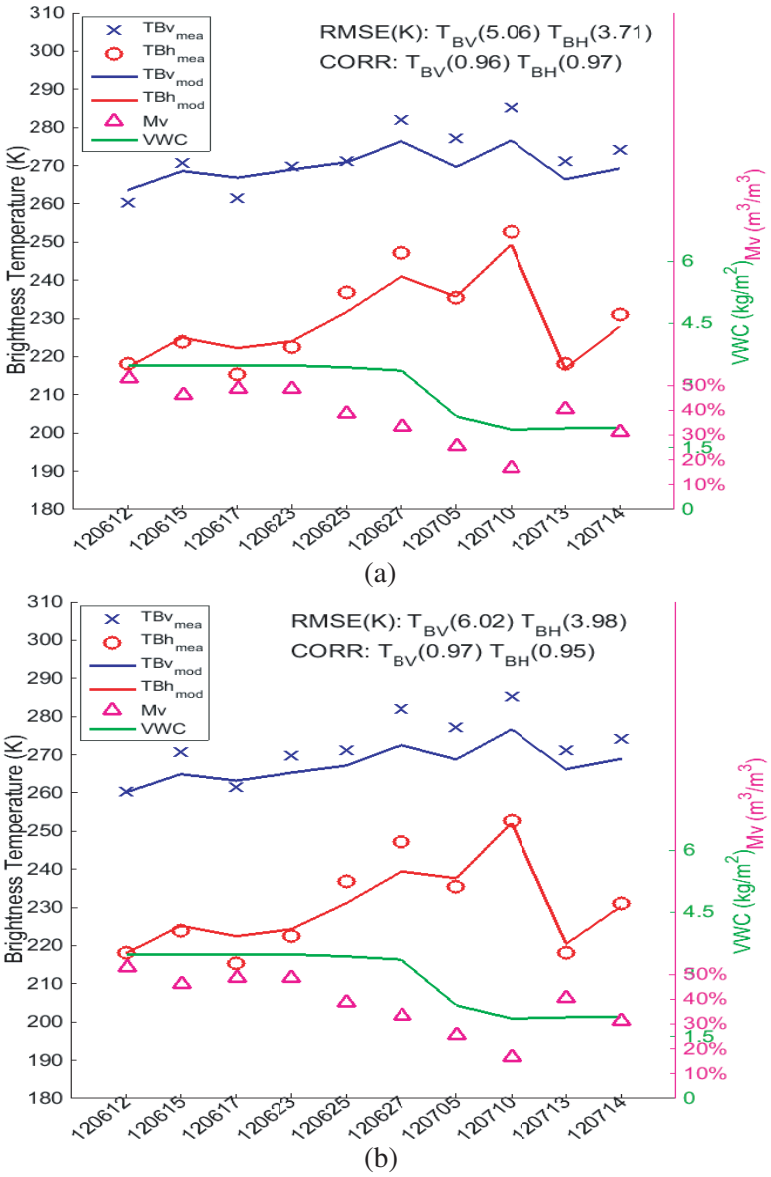

Figure 13. Model and measurement comparison of winter wheat field 941 for brightness temperature using (a) NMM3D-DBA, (b) tau-omega model. Soil surface RMS height is 1.10 cm.

where $\langle \kappa_s \rangle$ and $\langle \kappa_e \rangle$ are the scattering coefficient and extinction coefficient, respectively. $\langle \kappa_s \rangle$ and $\langle \kappa_e \rangle$ are calculated using the physical parameters as illustrated above. It is worth noting that the calculations of ω are not needed in the NMM3D-DBA model as shown in the derivations in Section 2 and ω is calculated here for comparison with the empirically chosen ω. The physically calculated ω depends on the size of the scatterers such as radius and length. As explained in Section 3, for wheat, winter wheat and canola, the size of the vegetation components (stalks, main stem and leaves) depends on VWC, thus ω also depends on VWC. The ω values for the wheat, winter wheat and canola fields in Table 6 are calculated at VWC equal to $2\,\mathrm{kg/m^2}$, which is a typical VWC value for these vegetation types.

For the τ parameter, if the physical ω is small, then the attenuation is dominated by the absorption, and the optical thickness τ of the vegetation layer is determined by the VWC and the b parameter, which is the proportionality constant between τ and VWC. However, if the physical ω is not small, then the b parameter also becomes non-physical. The physically calculated b and empirically adjusted b

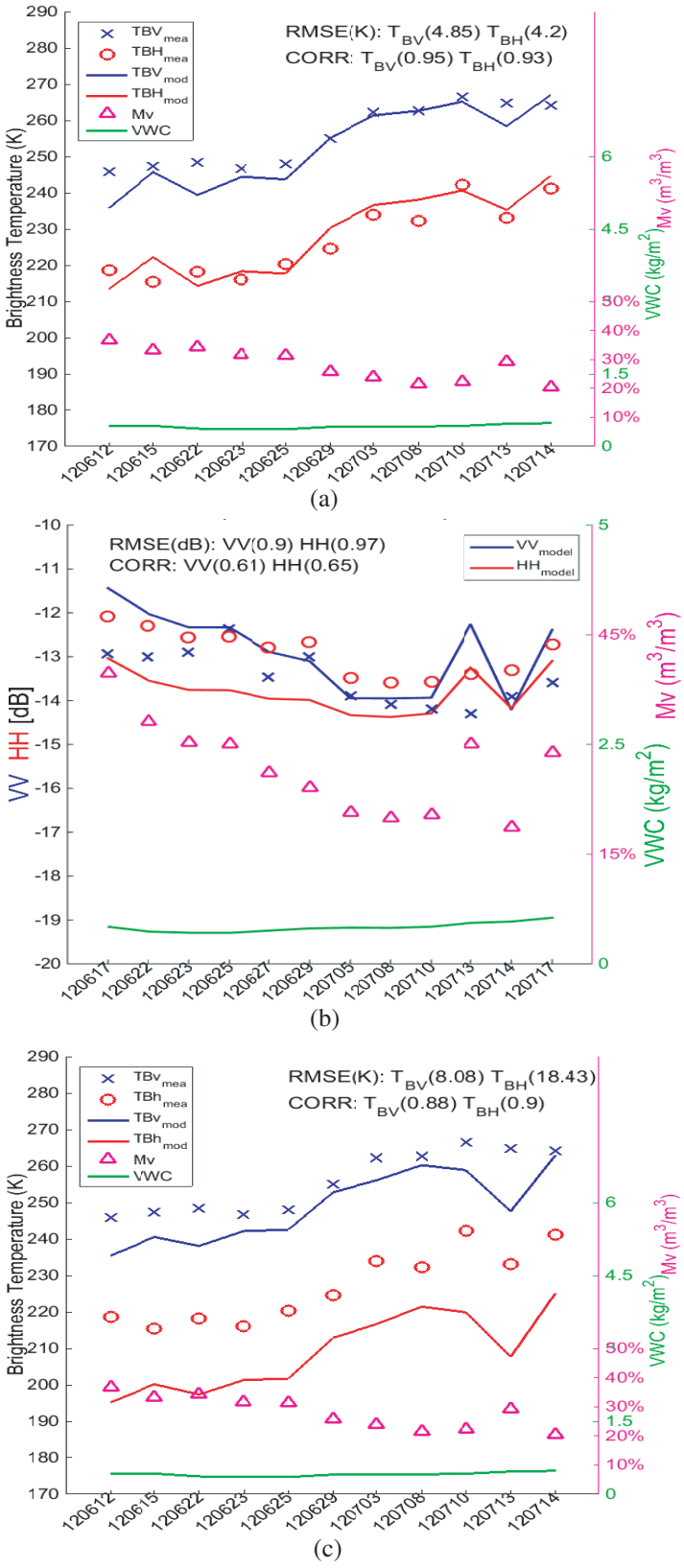

Figure 14. Model and measurement comparison of pasture field 21 for (a) brightness temperature using NMM3D-DBA, (b) backscatter using NMM3D-DBA, (c) brightness temperature using tau-omega model. Soil surface RMS height is 0.90 cm.

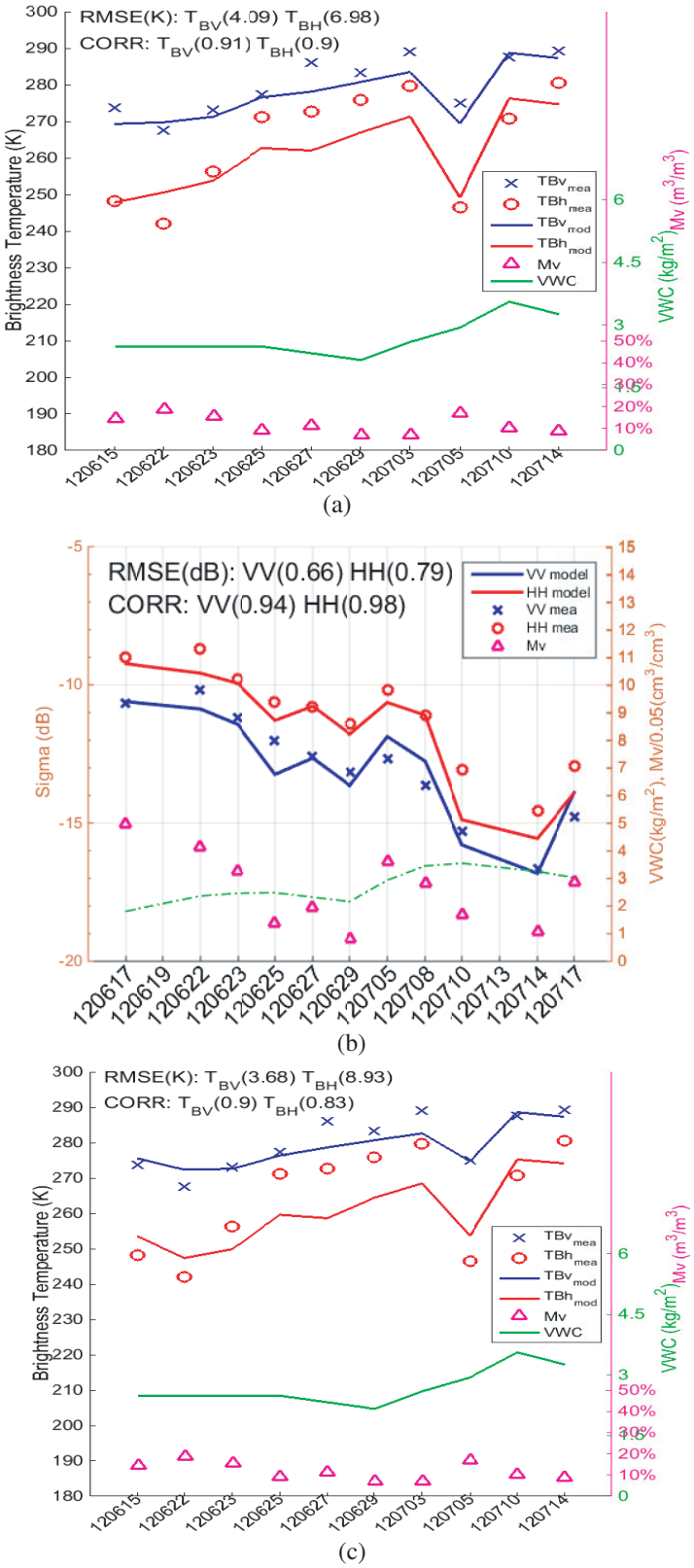

Figure 15. Model and measurement comparison of canola field 61 for (a) brightness temperature using NMM3D-DBA, (b) backscatter using NMM3D-DBA, (c) brightness temperature using tau-omega model. Soil surface RMS height is 1.00 cm.

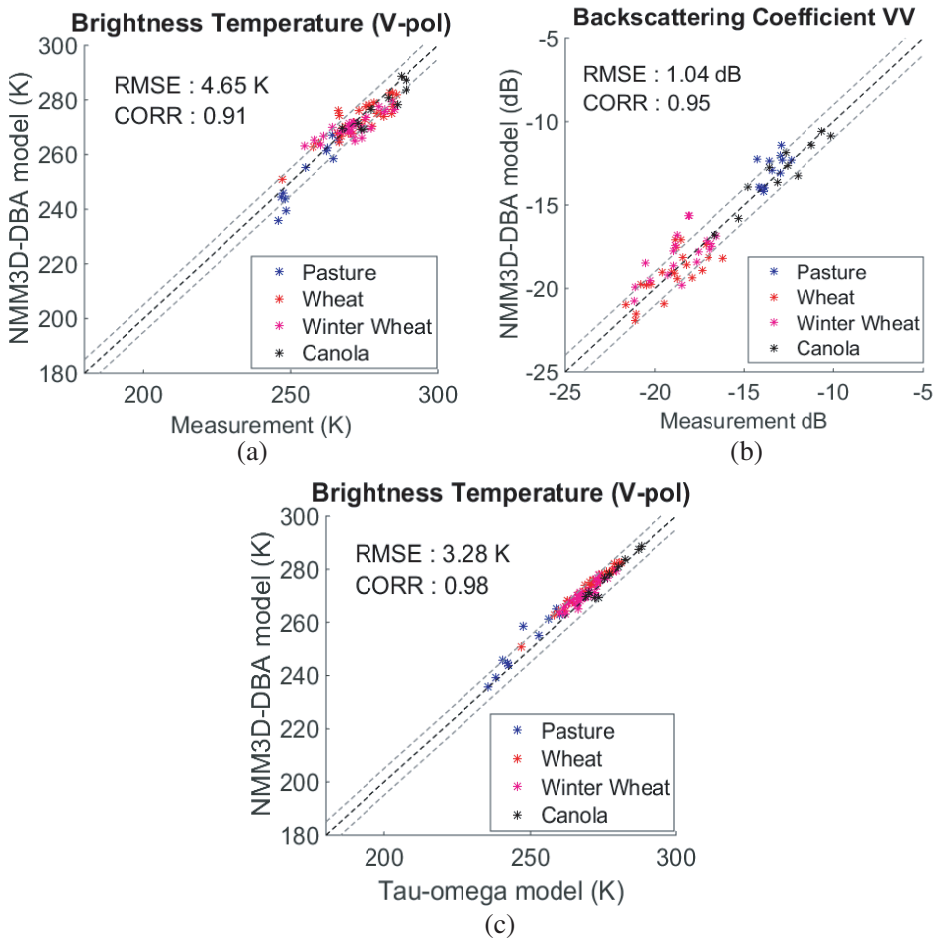

Figure 16. NMM3D-DBA model and measurement comparison of all the fields at vertical polarization for (a) brightness temperature TB (V-pol), (b) backscatter VV. (c) NMM3D-DBA model and tau-omega model comparison for brightness temperature TB (V-pol). The two grey dashed auxiliary lines in each plot are for $+/-5\,\mathrm{K}$ or $+/-1\,\mathrm{dB}$.

for SMAPVEX12 [30] are different and listed in Table 6. Physically, the optical thickness is defined as $\tau = \langle \kappa_e \rangle d$ [8] where d is the thickness of the vegetation layer. Then, the physically-based b is calculated as $b = \langle \kappa_e \rangle d/VWC$ using the physical parameters. It is worth noting that the calculations of b are not needed in the NMM3D-DBA model and b is calculated here for comparison with the empirically chosen b.

The tau-omega model rough surface parameters Q and h are also empirically tuned to fit the data. According to previous studies it is commonly assumed that $Q = 0$ at L-band [30]. In this case, h is adjusted based on soil moisture, precipitation events and soil texture [30] to best fit the PALS observations. In this paper, Equations (24) and (25) with $Q = 0$ are used for the tau-omega model for simplicity. When $r_p(\theta)$ for the tau-omega model is compared with the integration of $\langle S^R_{pq} S^{R*}_{pq} \rangle$ calculated from NMM3D in Equation (36), the results from NMM3D are generally larger than $r_p(\theta)$. This is because $r_p(\theta)$ only includes the coherent wave specular reflection [9] while ignoring the bistatic scattering. One example of a comparison between the result from NMM3D and the $r_p(\theta)$ used in the tau-omega model, under various soil moisture conditions and for an RMS height of 0.91 cm (field 91), is shown in Figure 19. It can be seen that regardless of the polarization, the results from NMM3D are larger than $r_p(\theta)$. It is also noticed that the results from the tau-omega model follow the same trend as those from the NMM3D which has several degrees more of complexity. This is because the coherent component along the specular direction dominates for rough surface with ks (product of the

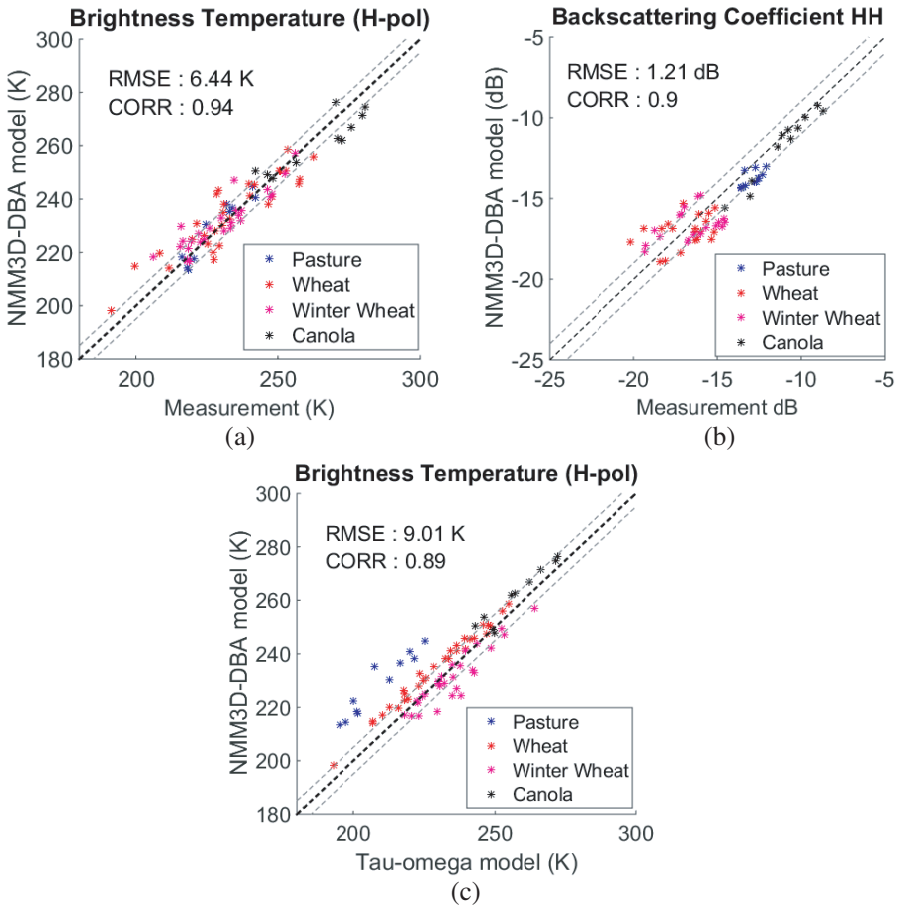

Figure 17. NMM3D-DBA model and measurement comparison of all the fields at horizontal polarization for (a) brightness temperature TB (H-pol), (b) backscatter HH. (c) NMM3D-DBA model and tau-omega model comparison for brightness temperature TB (H-pol). The two grey dashed auxiliary lines in each plot are for $+/-5\,\mathrm{K}$ or $+/-1\,\mathrm{dB}$.

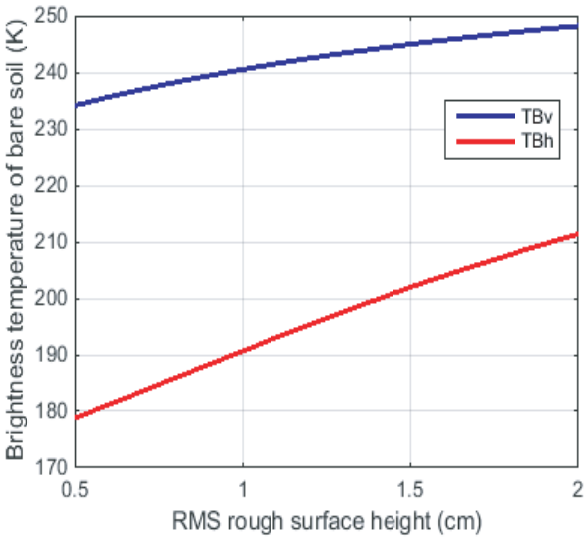

Figure 18. Brightness temperature change with RMS rough surface height for bare surface based on NMM3D.

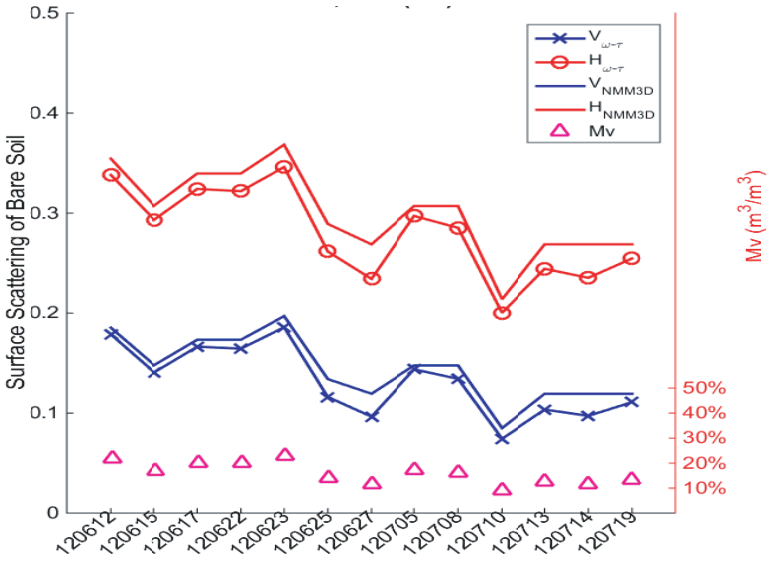

Figure 19. Comparison of (1-emissivity) for bare soil surface contribution between the tau-omega model and NMM3D-DBA for field 91 at *RMS* height 0.91 cm.

wavenumber and the *RMS* height, which is around 0.2 in this case) on the order of 0.1 [4] and the error from the neglection of non-coherent components along the bistatic directions in the tau-omega model is small in this case.

The tau-omega model brightness temperatures calculated using the empirical parameters for SMAPVEX12 [30] are compared with the PALS low-altitude radiometer data for each of the fields as shown in Figures 8–15. The results from tau-omega and NMM3D-DBA models for all the fields are also presented in the scatter plots in Figs. 16(c) and 17(c). The RMSE and correlation coefficient between the tau-omega model results and PALS observations are listed in Table 5 for comparison with the NMM3D-DBA. It can be seen that the results from the tau-omega and NMM3D-DBA are comparable to each other even though empirical parameters are used in the tau-omega model, while physical parameters are used in NMM3D-DBA. The RMSE is generally lower and the correlation coefficient (CORR) higher for the NMM3D-DBA than for the tau-omega model, indicating better agreement between measurement and model using the NMM3D-DBA, but this is not the case for all fields.

6. CONCLUSIONS

A consistent model for combined active and passive microwave remote sensing is formulated in which the same physical model NMM3D-DBA is used to calculate both backscatter and brightness temperature. The novel feature of this combined active and passive approach is its use of the same model NMM3D-DBA and physical parameters (such as crop density, plant height, stalk orientation, leaf radius, surface roughness, amongst others) for both active and passive for vegetated surfaces to achieve a consistent modelling framework. The NMM3D-DBA model allows the understanding that the defects in the vegetation modelling have more influence on the backscatter than the brightness temperature while the defects in the rough surface modelling have more influence on the brightness temperature than the backscatter, for the vegetation fields studied in this paper. In comparison, previous approaches generally use different models and different parameters for active and passive with the tau-omega model most frequently used as the passive model with empirical input parameters. The physical model combines the distorted Born approximation (DBA) with the NMM3D, including three scattering mechanisms: volume scattering, double bounce scattering and surface scattering. The distorted Born approximation is derived from the Foldy-Lax equation with first-order iteration using the half-space Green's function and T-matrix. NMM3D is used for the soil surface, which includes both the coherent

wave specular reflection and the bistatic scattering of the rough surface. The emissivity is obtained by integration of the bistatic scattering over the hemispherical solid angle. The NMM3D-DBA model results are validated using coincident airborne PALS low-altitude radiometer data and UAVSAR data taken during the SMAPVEX12 field campaign. For vertical polarization the averaged RMSE and correlation coefficient over all the fields are 4.65 K and 0.91 for brightness temperature and 1.04 dB and 0.95 for VV backscatter, while for horizontal polarization the average RMSE and correlation coefficient are 6.44 K and 0.94 for brightness temperature and 1.21 dB and 0.90 for HH backscatter. The uncertainty in the RMS height measurements can be one of the main sources of error for the modelled brightness temperature which strongly depends on the RMS height for the vegetated fields studied in this paper. The NMM3D-DBA model assumes the vegetation scatterers are uniformly distributed which is not strictly true for the crop fields. This assumption can also cause errors in the model. Overall, on comparisons with the passive data, the results from NMM3D-DBA are comparable or better than those from the tau-omega model. The tau-omega model uses empirically adjusted parameters though the empirical parameters, such as ω, which are different from the physically calculated values.

In the future, the vegetation structure will be modelled more accurately by taking into account the leaves and grains for wheat and using elliptical disks for canola leaves. The consistent combined active and passive model based on NMM3D-DBA adopts a single scattering model for vegetation; it has been shown to be able to provide good estimations for backscatter and brightness temperature at L-band for wheat, winter wheat, pasture, and canola fields. As the frequency increases, multiple scattering effects in vegetation become more important [26]. Thus, at frequencies much higher than L-band, a multiple scattering approach should be used for vegetation instead of the distorted Born approximation. We can use the same concept as presented in this paper to develop a consistent model for both active and passive at higher frequencies by using NMM3D for the soil surface together with a multiple scattering model for vegetation where the brightness temperature is calculated by integration of bistatic scattering coefficients. There are other vegetation types, such as soybean and corn, whose results are not presented here because the distorted Born approximation is not suitable for modelling them. Collective scattering effects of the vegetation scatterers are important for the soybean [38], thus a more accurate coherent model must be used for this vegetation type. For the corn field, multiple scattering effects [26] must be included because of the large scattering albedo and optical thickness. These two vegetation types and more accurate scattering models for higher frequencies will be studied in the future. Recently we have started the NMM3D full wave simulations of vegetation scattering [40]. Future work will consist of using NMM3D to replace the DBA part of the methodology of combined active and passive in this paper.

ACKNOWLEDGMENT

The authors would like to thank the SMAPVEX12 field campaign team for providing the measurement data. The research described in this paper was carried out at the University of Michigan, Ann Arbor, MI 48109, USA, and was supported in part by the Jet Propulsion Laboratory, California Institute of Technology, under a contract with the National Aeronautics and Space Administration.

APPENDIX A.

The appendix presents the derivations of the scattering matrix S from which the bistatic scattering coefficient γ is calculated with the use of Equation (5). As explained in Equation 3(b), the scattering fields include volume scattering and double bounce scattering which consists of two terms: scattering from the vegetation scatterer that is then reflected by the soil surface below (sr); and scattering of the reflected fields from the soil surface by the vegetation scatterer (rs).

$$\overline{E}_{s,j}^{vol} = \overline{\overline{G}}_{01}^{(0)} \overline{\overline{T}}_j \overline{E}_{inc} \tag{A1a}$$

$$\overline{E}_{s,j}^{db,sr} = \overline{\overline{G}}_{01}^{(R)} \overline{\overline{T}}_j \overline{E}_{inc} \tag{A1b}$$

$$\overline{E}_{s,j}^{db,rs} = \overline{\overline{G}}_{01}^{(0)} \overline{\overline{T}}_j \overline{E}_{ref} \tag{A1c}$$

where the superscript '*vol*' is short for volume scattering and '*db*' is short for double bounce scattering. The subscript "j" means it is for the jth scatterer. The incident and reflected fields are expressed as [8]

$$\overline{E}_{inc} = E_{iv}\hat{v}\left(\pi-\theta_i,\phi_i\right)\exp\left(i\overline{K}_{iv}\cdot\overline{r}\right)+E_{ih}\hat{h}\left(\pi-\theta_i,\phi_i\right)\exp\left(i\overline{K}_{ih}\cdot\overline{r}\right) \tag{A2}$$

$$\overline{E}_{ref} = \left[\begin{array}{l} E_{iv}R_v\left(\theta_i\right)\exp\left(2ik_{ivz}d\right)\hat{v}\left(\theta_i,\phi_i\right)\exp\left(i\overline{k}_{iv}\cdot\overline{r}\right) \\ +E_{ih}R_h\left(\theta_i\right)\exp\left(2ik_{ihz}d\right)\hat{h}\left(\theta_i,\phi_i\right)\exp\left(i\overline{k}_{ih}\cdot\overline{r}\right)\end{array}\right] \tag{A3}$$

with,

$$\overline{k}_{ip}=k\sin\theta_i\cos\phi_i\hat{x}+k\sin\theta_i\sin\phi_i\hat{y}+k_{ipz}\hat{z},\quad \overline{K}_{ip}=k\sin\theta_i\cos\phi_i\hat{x}+k\sin\theta_i\sin\phi_i\hat{y}-k_{ipz}\hat{z}$$

where $\hat{v}$ and $\hat{h}$ are the vertical and horizontal polarization directions, respectively. $\bar{r}$ is the observation point. R is the coherent reflectivity of the soil surface.

Using the stationary phase method for the far field [8], the two parts of Green's function are obtained as:

$$\overline{\overline{G}}_{01}^{(0)}\left(\overline{r},\overline{r}'\right) = \frac{\exp\left(ikr\right)}{4\pi r}\left[\begin{array}{l}\hat{h}\left(\theta_s,\phi_s\right)\hat{h}\left(\theta_s,\phi_s\right)\exp\left(-ik_{hz}z'\right) \\ +\hat{v}\left(\theta_s,\phi_s\right)\hat{v}\left(\theta_s,\phi_s\right)\exp\left(-ik_{vz}z'\right)\end{array}\right]\exp\left(-ik_xx'-ik_yy'\right) \tag{A4}$$

$$\begin{aligned}\overline{\overline{G}}_{01}^{(R)}\left(\overline{r},\overline{r}'\right) = {} & \frac{\exp\left(ikr\right)}{4\pi r}\left[\begin{array}{l}\hat{h}\left(\theta_s,\phi_s\right)R_h\left(\theta_s\right)\exp\left(2ik_{hz}d\right)\hat{h}\left(\pi-\theta_s,\phi_s\right)\exp\left(ik_{hz}z'\right) \\ +\hat{v}\left(\theta_s,\phi_s\right)R_v\left(\theta_s\right)\exp\left(2ik_{vz}d\right)\hat{v}\left(\pi-\theta_s,\phi_s\right)\exp\left(ik_{vz}z'\right)\end{array}\right] \\ & \exp\left(-ik_xx'-ik_yy'\right)\end{aligned} \tag{A5}$$

Substituting $\overline{\overline{G}}_{01}^{(0)}$ into Equation (A1a), the expression of volume scattering for scatterer j is:

$$\overline{E}_{s,j}^{vol}=\frac{\exp\left(ikr\right)}{4\pi r}\int d\overline{r}'\left[\begin{array}{l}\hat{h}\left(\theta_s,\phi_s\right)\hat{h}\left(\theta_s,\phi_s\right)\exp\left(-i\overline{k}_h\cdot\overline{r}'\right) \\ +\hat{v}\left(\theta_s,\phi_s\right)\hat{v}\left(\theta_s,\phi_s\right)\exp\left(-i\overline{k}_v\cdot\overline{r}'\right)\end{array}\right]\int d\overline{r}''\left\langle\overline{r}'\left|T_j\right|\overline{r}''\right\rangle\left\langle\overline{r}''|\overline{E}_{inc}\right\rangle \tag{A6}$$

where r is the distance of the observation point.

In calculations of Equation (A6), momentum representation is used [8]. The momentum representation of a function is closely related to the Fourier transform of the function in position space. Since we know the relationship between the momentum representation of the T-matrix and the scattering amplitude of a scatterer [8] (as presented later in Equation (A8)), the T-matrix in momentum space is used rather than in position space. Substituting $\overline{E}_{inc}$ and after some calculations, volume scattering for scatterer j at $\overline{r}_j$ is expressed as:

$$\begin{aligned}\overline{E}_{s,j}^{vol} = {} & \frac{\exp\left(ikr\right)}{4\pi r}\left[\hat{v}\left(\theta_s,\phi_s\right)\hat{v}\left(\theta_s,\phi_s\right)\right]\exp\left(-i\left(\overline{k}_{sv}-\overline{K}_{iv}\right)\cdot\overline{r}_j\right)\cdot\overline{\overline{T}}_j\left(\overline{k}_{sv},\overline{K}_{iv}\right)\cdot\left[E_{iv}\hat{v}\left(\pi-\theta_i,\phi_i\right)\right] \\ & +\frac{\exp\left(ikr\right)}{4\pi r}\left[\hat{h}\left(\theta_s,\phi_s\right)\hat{h}\left(\theta_s,\phi_s\right)\right]\exp\left(-i\left(\overline{k}_{sh}-\overline{K}_{iv}\right)\cdot\overline{r}_j\right)\cdot\overline{\overline{T}}_j\left(\overline{k}_{sh},\overline{K}_{iv}\right)\cdot\left[E_{iv}\hat{v}\left(\pi-\theta_i,\phi_i\right)\right] \\ & +\frac{\exp\left(ikr\right)}{4\pi r}\left[\hat{v}\left(\theta_s,\phi_s\right)\hat{v}\left(\theta_s,\phi_s\right)\right]\exp\left(-i\left(\overline{k}_{sv}-\overline{K}_{ih}\right)\cdot\overline{r}_j\right)\cdot\overline{\overline{T}}_j\left(\overline{k}_{sv},\overline{K}_{ih}\right)\cdot\left[E_{ih}\hat{h}\left(\pi-\theta_i,\phi_i\right)\right] \\ & +\frac{\exp\left(ikr\right)}{4\pi r}\left[\hat{h}\left(\theta_s,\phi_s\right)\hat{h}\left(\theta_s,\phi_s\right)\right]\exp\left(-i\left(\overline{k}_{sh}-\overline{K}_{ih}\right)\cdot\overline{r}_j\right)\cdot\overline{\overline{T}}_j\left(\overline{k}_{sh},\overline{K}_{ih}\right)\cdot\left[E_{ih}\hat{h}\left(\pi-\theta_i,\phi_i\right)\right]\end{aligned} \tag{A7}$$

The relationship between T-matrix and scattering amplitude [8] is:

$$f_{pq,j}\left(\theta_s,\phi_s;\theta_i,\phi_i\right)=\frac{1}{4\pi}\hat{p}\left(\theta_s,\phi_s\right)\cdot\overline{\overline{T}}_j\left(\overline{k}_{sp},\overline{K}_{iq}\right)\cdot\hat{q}\left(\theta_i,\phi_i\right) \tag{A8}$$

Substituting (A8) into (A7), the volume scattering for all the N scatterers is obtained as:

$$\overline{E}_s^{vol}=\frac{\exp\left(ikr\right)}{r}\left[\hat{v}\left(\theta_s,\phi_s\right)S_{vv}^{vol}E_{iv}+\hat{h}\left(\theta_s,\phi_s\right)S_{hv}^{vol}E_{iv}+\hat{v}\left(\theta_s,\phi_s\right)S_{vh}^{vol}E_{ih}+\hat{h}\left(\theta_s,\phi_s\right)S_{hh}^{vol}E_{ih}\right] \tag{A9}$$

$$\text{with, }\ S_{pq}^{vol}=\sum_{j=1}^{N}\exp\left(-i\left(\overline{k}_{sp}-\overline{K}_{iq}\right)\cdot\overline{r}_j\right)f_{pq,j}\left(\theta_s,\phi_s;\pi-\theta_i,\phi_i\right) \tag{A10}$$

Next, we calculate the scattering matrix for the first term of the double bounce scattering (scattering from the vegetation scatterer that is then reflected by the soil surface below (sr)). Substituting $\overline{\overline{G}}_{01}^{(R)}$ as in Equation (A5) into Equation (A1b), the following relationship is obtained:

$$\overline{E}_{s,j}^{db,sr} = \frac{\exp(ikr)}{4\pi r}\int d\overline{r}' \begin{bmatrix} \hat{h}(\theta_s,\phi_s) R_h(\theta_s) \exp(2ik_{hz}d)\, \hat{h}(\pi-\theta_s,\phi_s) \exp\left(-i\overline{K}_h\cdot\overline{r}'\right) \\ +\hat{v}(\theta_s,\phi_s) R_v(\theta_s) \exp(2ik_{vz}d)\, \hat{v}(\pi-\theta_s,\phi_s) \exp\left(-i\overline{K}_v\cdot\overline{r}'\right) \end{bmatrix} \times \int d\overline{r}'' \left\langle \overline{r}' \left| T_j \right| \overline{r}'' \right\rangle \left\langle \overline{r}'' | \overline{E}_{inc} \right\rangle \quad \text{(A11)}$$

Substituting $\overline{E}_{inc}$ and calculating in the same way used for volume scattering above, Equation (A11) becomes:

$$\overline{E}_{s,j}^{db,sr} = \frac{\exp(ikr)}{4\pi r} \times \begin{Bmatrix} [\hat{v}(\theta_s,\phi_s) R_v(\theta_s) \exp(2ik_{svz}d)\, \hat{v}(\pi-\theta_s,\phi_s)] \exp\left(-i\left(\overline{K}_{sv}-\overline{K}_{iv}\right)\cdot\overline{r}_j\right)\cdot\overline{\overline{T}}_j\left(\overline{K}_{sv},\overline{K}_{iv}\right)\cdot[E_{iv}\hat{v}(\pi-\theta_i,\phi_i)] \\ +\left[\hat{h}(\theta_s,\phi_s) R_h(\theta_s) \exp(2ik_{shz}d)\, \hat{h}(\pi-\theta_s,\phi_s)\right] \exp\left(-i\left(\overline{K}_{sh}-\overline{K}_{iv}\right)\cdot\overline{r}_j\right)\cdot\overline{\overline{T}}_j\left(\overline{K}_{sh},\overline{K}_{iv}\right)\cdot[E_{iv}\hat{v}(\pi-\theta_i,\phi_i)] \\ +[\hat{v}(\theta_s,\phi_s) R_v(\theta_s) \exp(2ik_{svz}d)\, \hat{v}(\pi-\theta_s,\phi_s)] \exp\left(-i\left(\overline{K}_{sv}-\overline{K}_{ih}\right)\cdot\overline{r}_j\right)\cdot\overline{\overline{T}}_j\left(\overline{K}_{sv},\overline{K}_{ih}\right)\cdot\left[E_{ih}\hat{h}(\pi-\theta_i,\phi_i)\right] \\ +\left[\hat{h}(\theta_s,\phi_s) R_h(\theta_s) \exp(2ik_{shz}d)\, \hat{h}(\pi-\theta_s,\phi_s)\right] \exp\left(-i\left(\overline{K}_{sh}-\overline{K}_{ih}\right)\cdot\overline{r}_j\right)\cdot\overline{\overline{T}}_j\left(\overline{K}_{sh},\overline{K}_{ih}\right)\cdot\left[E_{ih}\hat{h}(\pi-\theta_i,\phi_i)\right] \end{Bmatrix} \quad \text{(A12)}$$

Using Equation (A8), we obtain the following:

$$\overline{E}_s^{db,sr} = \frac{\exp(ikr)}{r}\left[\hat{v}(\theta_s,\phi_s) S_{vv}^{db,sr} E_{iv} + \hat{h}(\theta_s,\phi_s) S_{hv}^{db,sr} E_{iv} + \hat{v}(\theta_s,\phi_s) S_{vh}^{db,sr} E_{ih} + \hat{h}(\theta_s,\phi_s) S_{hh}^{db,sr} E_{ih}\right] \quad \text{(A13)}$$

$$\text{with } S_{pq}^{db,sr} = \sum_{j=1}^{N} R_p(\theta_s) \exp(2ik_{spz}d) \exp\left(-i\left(\overline{K}_{sp}-\overline{K}_{iq}\right)\cdot\overline{r}_j\right) f_{pq}(\pi-\theta_s,\phi_s;\pi-\theta_i,\phi_i) \quad \text{(A14)}$$

Similarly, for the other term of the double bounce scattering (scattering of the reflected fields from the soil surface by the vegetation scatterer (rs)), we substitute $\overline{\overline{G}}_{01}^{(0)}$ as in Equation (A4) into the third term of Equation (A1c). It is obtained that:

$$\overline{E}_{s,j}^{db,rs} = \frac{\exp(ikr)}{4\pi r}\int d\overline{r}' \begin{bmatrix} \hat{h}(\theta_s,\phi_s)\, \hat{h}(\theta_s,\phi_s) \exp\left(-i\overline{k}_h\cdot\overline{r}'\right) \\ +\hat{v}(\theta_s,\phi_s)\, \hat{v}(\theta_s,\phi_s) \exp\left(-i\overline{k}_v\cdot\overline{r}'\right) \end{bmatrix} \int d\overline{r}'' \left\langle \overline{r}' \left| T_j \right| \overline{r}'' \right\rangle \left\langle \overline{r}'' | \overline{E}_{ref} \right\rangle \quad \text{(A15)}$$

Substituting $\overline{E}_{ref}$ as in Equation (A3), Equation (A15) is calculated to:

$$\overline{E}_{s,j}^{db,rs} = \frac{\exp(ikr)}{4\pi r} \times \begin{Bmatrix} [\hat{v}(\theta_s,\phi_s)\, \hat{v}(\theta_s,\phi_s) R_v(\theta_i) \exp(2ik_{ivz}d)] \exp\left(-i\left(\overline{k}_{sv}-\overline{k}_{iv}\right)\cdot\overline{r}_j\right)\cdot\overline{\overline{T}}_j\left(\overline{k}_{sv},\overline{k}_{iv}\right)\cdot[E_{iv}\hat{v}(\theta_i,\phi_i)] \\ +\left[\hat{h}(\theta_s,\phi_s)\, \hat{h}(\theta_s,\phi_s) R_v(\theta_i) \exp(2ik_{ivz}d)\right] \exp\left(-i\left(\overline{k}_{sh}-\overline{k}_{iv}\right)\cdot\overline{r}_j\right)\cdot\overline{\overline{T}}_j\left(\overline{k}_{sh},\overline{k}_{iv}\right)\cdot[E_{iv}\hat{v}(\theta_i,\phi_i)] \\ +[\hat{v}(\theta_s,\phi_s)\, \hat{v}(\theta_s,\phi_s) R_h(\theta_i) \exp(2ik_{ihz}d)] \exp\left(-i\left(\overline{k}_{sv}-\overline{k}_{ih}\right)\cdot\overline{r}_j\right)\cdot\overline{\overline{T}}_j\left(\overline{k}_{sv},\overline{k}_{ih}\right)\cdot\left[E_{ih}\hat{h}(\theta_i,\phi_i)\right] \\ +\left[\hat{h}(\theta_s,\phi_s)\, \hat{h}(\theta_s,\phi_s) R_h(\theta_i) \exp(2ik_{ihz}d)\right] \exp\left(-i\left(\overline{k}_{sh}-\overline{k}_{ih}\right)\cdot\overline{r}_j\right)\cdot\overline{\overline{T}}_j\left(\overline{k}_{sh},\overline{k}_{ih}\right)\cdot\left[E_{ih}\hat{h}(\theta_i,\phi_i)\right] \end{Bmatrix} \quad \text{(A16)}$$

Using the relationship between T-matrix and scattering amplitude results in the following Equation:

$$\overline{E}_s^{db,rs} = \frac{\exp(ikr)}{r}\left[\hat{v}(\theta_s,\phi_s) S_{vv}^{db,rs} E_{iv} + \hat{h}(\theta_s,\phi_s) S_{hv}^{db,rs} E_{iv} + \hat{v}(\theta_s,\phi_s) S_{vh}^{db,rs} E_{ih} + \hat{h}(\theta_s,\phi_s) S_{hh}^{db,rs} E_{ih}\right] \quad \text{(A17)}$$

$$\text{with } S_{pq}^{db,rs} = \sum_{j=1}^{N} R_q(\theta_i) \exp(2ik_{iqz}d) \exp\left(-i\left(\overline{k}_{sp}-\overline{k}_{iq}\right)\cdot\overline{r}_j\right) f_{pq}(\theta_s,\phi_s;\theta_i,\phi_i) \quad \text{(A18)}$$

REFERENCES

1. Entekhabi, D., E. G. Njoku, P. E. O'Neill, K. H. Kellogg, W. T. Crow, W. N. Edelstein, et al., "The Soil Moisture Active Passive (SMAP) mission," *Proceedings of the IEEE*, Vol. 98, 704–716, May 2010.

2. Jackson, T. J. and T. J. Schmugge, "Vegetation effects on the microwave emission of soils," *Remote Sensing of Environment*, Vol. 36, 203–212, Jun. 1991.
3. Monerris, A. and T. Schmugge, "Soil moisture estimation using L-band radiometry," *Advances in Geoscience and Remote Sensing*, InTech, 2009.
4. Ulaby, F. T., D. G. Long, W. J. Blackwell, C. Elachi, A. K. Fung, C. Ruf, et al., *Microwave Radar and Radiometric Remote Sensing*, University of Michigan Press, 2014.
5. Entekhabi, D., S. Yueh, P. O'Neill, and K. Kellogg, *SMAP Handbook*, 400–1567, JPL Publication JPL, 2014.
6. Kerr, Y. H. and E. G. Njoku, "A semiempirical model for interpreting microwave emission from semiarid land surfaces as seen from space," *IEEE Transactions on Geoscience and Remote Sensing*, Vol. 28, 384–393, 1990.
7. Jackson, T. and T. Schmugge, "Vegetation effects on the microwave emission of soils," *Remote Sensing of Environment*, Vol. 36, 203–212, 1991.
8. Tsang, L., J. A. Kong, and R. T. Shin, *Theory of Microwave Remote Sensing*, Wiley, New York, 1985.
9. Oh, Y., K. Sarabandi, and F. T. Ulaby, "Semi-empirical model of the ensemble-averaged differential Mueller matrix for microwave backscattering from bare soil surfaces," *IEEE Transactions on Geoscience and Remote Sensing*, Vol. 40, 1348–1355, Jun. 2002.
10. Lang, R. H. and J. S. Sidhu, "Electromagnetic backscattering from a layer of vegetation — A discrete approach," *IEEE Transactions on Geoscience and Remote Sensing*, Vol. 21, 62–71, 1983.
11. Huang, S. and L. Tsang, "Electromagnetic scattering of randomly rough soil surfaces based on numerical solutions of Maxwell equations in three-dimensional simulations using a hybrid UV/PBTG/SMCG method," *IEEE Transactions on Geoscience and Remote Sensing*, Vol. 50, 4025–4035, 2012.
12. Kim, S. B., L. Tsang, J. T. Johnson, S. Huang, J. J. van Zyl, and E. G. Njoku, "Soil moisture retrieval using time-series radar observations over bare surfaces," *IEEE Transactions on Geoscience and Remote Sensing*, Vol. 50, 1853–1863, May 2012.
13. Kim, S.-B., M. Moghaddam, L. Tsang, M. Burgin, X. Xu, and E. G. Njoku, "Models of L-band radar backscattering coefficients over global terrain for soil moisture retrieval," *IEEE Transactions on Geoscience and Remote Sensing*, Vol. 52, 1381–1396, 2014.
14. McNairn, H., T. J. Jackson, G. Wiseman, S. Belair, A. Berg, P. Bullock, et al., "The Soil Moisture Active Passive Validation Experiment 2012 (SMAPVEX12): Prelaunch calibration and validation of the SMAP soil moisture algorithms," *IEEE Transactions on Geoscience and Remote Sensing*, Vol. 53, 2784–2801, 2015.
15. Bolten, J. D., V. Lakshmi, and E. G. Njoku, "Soil moisture retrieval using the passive/active L- and S-band radar/radiometer," *IEEE Transactions on Geoscience and Remote Sensing*, Vol. 41, 2792–2801, Dec. 2003.
16. Bindlish, R., T. Jackson, R. J. Sun, M. Cosh, S. Yueh, and S. Dinardo, "Combined passive and active microwave observations of soil moisture during CLASIC," *IEEE Geoscience and Remote Sensing Letters*, Vol. 6, 644–648, Oct. 2009.
17. Ferrazzoli, P., G. Luzi, S. Paloscia, P. Pampaloni, G. Schiavon, and D. Solimini, "Comparison between the microwave emissivity and backscatter coefficient of crops," *IEEE Transactions on Geoscience and Remote Sensing*, Vol. 27, 772–778, Nov. 1989.
18. Guerriero, L., P. Ferrazzoli, and R. Rahmoune, "A synergyc view of L-band active and passive remote sensing of vegetated soil," *2012 12th Specialist Meeting on Microwave Radiometry and Remote Sensing of the Environment (MicroRad)*, 1–3, 2012.
19. Chauhan, N. S. and D. M. Levine, "Discrete scatter model for microwave radar and radiometer response to corn — Comparison of theory and data," *IEEE Transactions on Geoscience and Remote Sensing*, Vol. 32, 416–426, Mar. 1994.

20. Lang, R. H., "Scattering from a layer of discrete random medium over a random interface: application to microwave backscattering from forests," *Waves in Random Media*, Vol. 14, S359–S391, Apr. 2004.
21. Yueh, S. H., J. A. Kong, J. K. Jao, R. T. Shin, and T. Letoan, "Branching model for vegetation," *IEEE Transactions on Geoscience and Remote Sensing*, Vol. 30, 390–402, Mar. 1992.
22. Stiles, J. M. and K. Sarabandi, "Electromagnetic scattering from grassland Part I: A fully phase-coherent scattering model," *IEEE Transactions on Geoscience and Remote Sensing*, Vol. 38, 339–348, Jan. 2000.
23. Stiles, J. M., K. Sarabandi, and F. T. Ulaby, "Electromagnetic scattering from grassland Part II: Measurement and modelling results," *IEEE Transactions on Geoscience and Remote Sensing*, Vol. 38, 349–356, Jan. 2000.
24. Ulaby, F. T., K. Sarabandi, K. Mcdonald, M. Whitt, and M. C. Dobson, "Michigan microwave canopy scattering model," *International Journal of Remote Sensing*, Vol. 11, 1223–1253, Jul. 1990.
25. Tsang, L., J. Kong, and K.-H. Ding, *Scattering of Electromagnetic Waves: Theories and Applications*, John Wisley & Sons, ed: Inc, 2000.
26. Liao, T.-H., S. B. Kim, S. R. Tan, L. Tsang, C. X. Su, and T. J. Jackson, "Multiple scattering effects with cyclical correction in active remote sensing of vegetated surface using vector radiative transfer theory," *IEEE Journal of Selected Topics in Applied Earth Observations and Remote Sensing*, Vol. 9, 1414–1429, Apr. 2016.
27. Toure, A., K. P. B. Thomson, G. Edwards, R. J. Brown, and B. G. Brisco, "Adaptation of the mimics backscattering model to the agricultural context — Wheat and canola at L and C bands," *IEEE Transactions on Geoscience and Remote Sensing*, Vol. 32, 47–61, Jan. 1994.
28. Huang, S. W., L. Tsang, E. G. Njoku, and K. S. Chan, "Backscattering coefficients, coherent reflectivities, and emissivities of randomly rough soil surfaces at L-band for SMAP applications based on numerical solutions of maxwell equations in three-dimensional simulations," *IEEE Transactions on Geoscience and Remote Sensing*, Vol. 48, 2557–2568, Jun. 2010.
29. Njoku, E. G. and D. Entekhabi, "Passive microwave remote sensing of soil moisture," *Journal of Hydrology*, Vol. 184, 101–129, Oct. 1, 1996.
30. Colliander, A., E. G. Njoku, T. J. Jackson, S. Chazanoff, H. McNairn, and J. Powers, "Retrieving soil moisture for non-forested areas using PALS radiometer measurements in SMAPVEX12 field campaign," *Remote Sensing of Environment*, Vol. 184, 86–100, Oct. 2016.
31. Hensley, S., K. Wheeler, G. Sadowy, C. Jones, S. Shaffer, H. Zebker, et al., "The UAVSAR instrument: Description and first results," *2008 IEEE Radar Conference*, Vols. 1–4, 827–832, 2008.
32. Mladenova, I. E., T. J. Jackson, R. Bindlish, and S. Hensley, "Incidence angle normalization of radar backscatter data," *IEEE Transactions on Geoscience and Remote Sensing*, Vol. 51, 1791—1804, Mar. 2013.
33. Colliander, A., T. Jackson, H. McNairn, S. Chazanoff, S. Dinardo, B. Latham, et al., "Comparison of airborne Passive and Active L-band System (PALS) brightness temperature measurements to SMOS observations during the SMAP Validation Experiment 2012 (SMAPVEX12)," *IEEE Geoscience and Remote Sensing Letters*, Vol. 12, 801–805, Apr. 2015.
34. Jester, W. and A. Klik, "Soil surface roughness measurement — Methods, applicability, and surface representation," *Catena*, Vol. 64, 174–192, Dec. 30, 2005.
35. Rowlandson, T. L., A. A. Berg, P. R. Bullock, E. R. Ojo, H. McNairn, G. Wiseman, et al., "Evaluation of several calibration procedures for a portable soil moisture sensor," *Journal of Hydrology*, Vol. 498, 335–344, Aug. 19, 2013.
36. Cosh, M. H., T. J. Jackson, R. Bindlish, J. S. Famiglietti, and D. Ryu, "Calibration of an impedance probe for estimation of surface soil water content over large regions," *Journal of Hydrology*, Vol. 311, 49–58, Sep. 15, 2005.
37. Ulaby, F. T. and M. A. Elrayes, "Microwave dielectric spectrum of vegetation. 2. Dual-dispersion model," *IEEE Transactions on Geoscience and Remote Sensing*, Vol. 25, 550–557, Sep. 1987.

38. Huang, H., S.-B. Kim, L. Tsang, X. Xu, T.-H. Liao, T. J. Jackson, et al., "Coherent model of L-band radar scattering by soybean plants: Model development, evaluation, and retrieval," *IEEE Journal of Selected Topics in Applied Earth Observations and Remote Sensing*, Vol. 9, No. 1, 272–284, Jan. 2016.
39. Njoku, E. G. and J. A. Kong, "Theory for passive microwave remote-sensing of near-surface soil-moisture," *Transactions-American Geophysical Union*, Vol. 58, 554–554, 1977.
40. Huang, H., L. Tsang, E. G. Njoku, A. Colliander, T.-H. Liao, and K.-H. Ding, "Propagation and scattering by a layer of randomly distributed dielectric cylinders using monte carlo simulations of 3D Maxwell equations with applications in microwave interactions with vegetation," *IEEE Access*, Vol. 5, 11985–12003, 2017.